



Zero-thermal-expansion metamaterial with broadband vibration suppression

Dewen Yu^{a,b}, Guobiao Hu^{c,*}, Wei Ding^d, Yaowen Yang^{b,*}, Jun Hong^a

^a Key Laboratory of Education Ministry for Modern Design and Rotor-Bearing System, School of Mechanical Engineering, Xi'an Jiaotong University, Xianning West Road, Xi'an 710049, China

^b School of Civil and Environmental Engineering, Nanyang Technological University, Nanyang Avenue Singapore 639798, Singapore

^c Internet of Things Thrust, The Hong Kong University of Science and Technology (Guangzhou), Nansha, Guangzhou, Guangdong 511400, China

^d State Key Laboratory of Strength and Vibration of Mechanical Structures, School of Mechanical Engineering, Xi'an Jiaotong University, Xianning West Road, Xi'an 710049, China



ARTICLE INFO

Keywords:

Metamaterial
Thermal expansion
Vibration attenuation
Band gap
Spectral element method
Star-shaped lattice structure

ABSTRACT

Although conventional metamaterials possess extraordinary properties, they cannot meet the practical requirements of engineering structures subjected to both temperature fluctuations and vibration excitations. To bridge this research gap, this paper proposes a novel dual-functional metamaterial with zero thermal expansion and broadband vibration suppression. Inspired by the thermal mismatch and band gap effects, we present an innovative design strategy that incorporates star-shaped re-entrant lattices and locally rudder-shaped struts with two-phase materials. To effectively guide the coupled design, a theoretical model accounting for stretching-bending deformations is established to predict the thermoelastic behavior of the metamaterial. Moreover, a parameterized dynamic model using the spectral element method is developed to study the vibration characteristics. Particularly, the spectral formulation of curved Timoshenko beams is derived, including in-plane and out-of-plane vibrations. The comparisons between theoretical predictions and finite element simulations validate the accuracy of analytical models in characterizing thermal deformations and vibration responses. Finally, the case studies shed light on the underlying formation mechanisms of zero thermal expansion and multiple band gaps, while also unveiling the effects of geometric parameters on the performance of such dual-functional metamaterials. Our innovative design strategy and analytical methodology not only offer appealing alternatives for engineering applications but also push the boundaries of metamaterial properties by enabling the transition from single- to dual-functionality.

1. Introduction

Manipulating structural deformation and vibration responses is of paramount significance across numerous high-level engineering applications [1,2]. Taking extendible support structures [3] of satellite antennas as an example, they inevitably suffer from drastic temperature swings and various dynamic loadings in outer space [4]. External stimuli may induce excessive thermal deformation and undesired structural deformation/vibration, resulting in accuracy degradation and even system failure. Particularly, it is worth noting that these external stimuli applied to structures are generally stochastic and time-space dependent. It is challenging or even infeasible to design an additional controller for effectively regulating the structural responses [5]. Therefore, a natural concern is whether structures can be endowed with extraordinary

mechanical properties that enable them to smartly accommodate complex shifting scenarios, such as zero thermal expansion and vibration self-attenuation [6].

It is still an indisputable fact that zero thermal expansion does not exist in naturally occurring or traditionally manufactured materials. Fortunately, the emergence of metamaterials gives birth to the possibility of customizing coefficients of thermal expansion (CTE). There are two main strategies to change CTE from negative to positive. One strategy is to utilize supramolecular mechanisms [7], e.g., phonon modes and phase transitions [8], to adjust the CTE. However, the desired thermal properties are achieved under harsh conditions at the cost of robustness and durability [9], which seriously limits their practical applications [10]. The second strategy relies on carefully engineering composite structures with different constituent materials [11], in which

* Corresponding authors.

E-mail addresses: guobiaohu@hkust-gz.edu.cn (G. Hu), ywyang@ntu.edu.sg (Y. Yang).

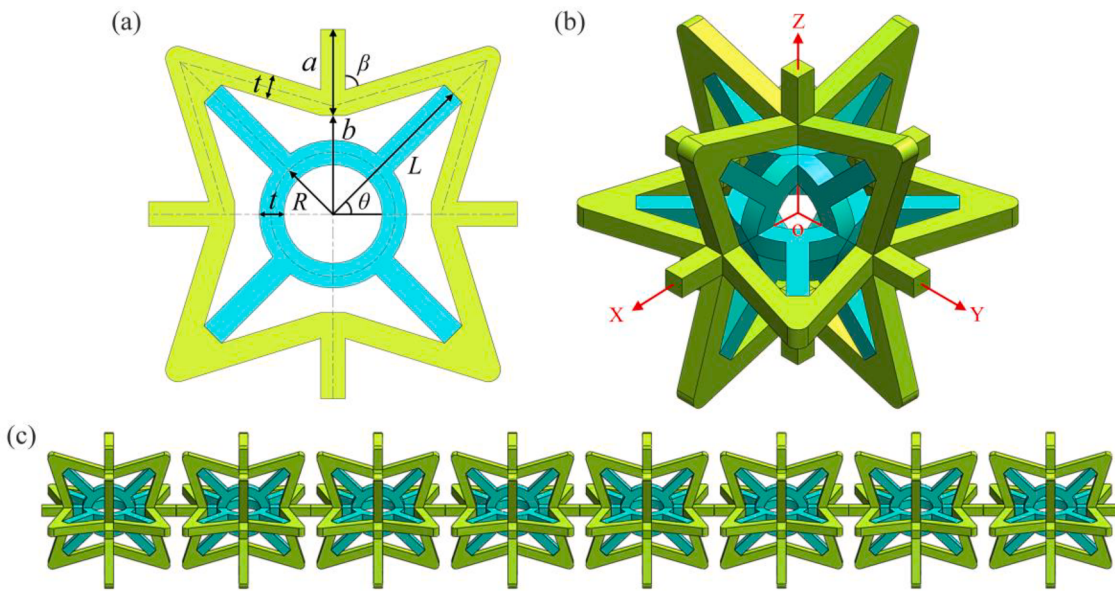


Fig. 1. Schematic of the 3D dual-functional metamaterial. (a) 2D unit cell; (b) 3D unit cell; (c) Thermoelastic metamaterial with the periodically arrayed unit cells. In this design, each metamaterial unit cell consists of exterior star-shaped re-entrant lattices and interior rudder-shaped reinforced struts. Additionally, two colors are used to characterize two metallic materials with distinct CTEs.

the thermal mismatch can lead to contractionary deformation. To ensure high stability and reliability [12], different deformation modes have been introduced into metamaterials to achieve a wide range of tunable CTE.

Recent studies on mechanical metamaterials have shown that the ideal CTE can be achieved by ingenious microstructure design and appropriate constituent selection [13–15]. Inspired by the thermal shrinkage mechanism of ZrW_2O_8 [16], Jefferson *et al.* [17] designed a hexagonal grid structure to counteract the expansion effect with the flexural rotation of two Lakes-type bending components. Lehman *et al.* [18] and Ha *et al.* [19] showed that tuning the geometric parameters of bi-material curved ribs is an effective way to obtain desired thermal properties. According to the uncoordinated deformation principle of bi-material beams, other bending-dominated architectures, such as re-entrant honeycombs [20] and polytope sectors [21], could also exhibit tailorable CTE. Though such bending-dominated metamaterials have wider tunable CTE [22], their mechanical properties are inferior to those of stretching-dominated counterparts [23,24]. After all, thermally induced stresses are dominantly determined by axial forces. For this reason, Wei *et al.* [25,26] utilized a bi-material diamond lattice to construct various stretching-dominated metamaterials with programmable CTE. In a word, the structure-thermal property relationships have been investigated for stretching-dominated metamaterials that are composed of star-square networks [27], pyramid-tetrahedron unit cells [28], octet-truss lattices [29], etc. By employing distinct spatial tessellations in planar configurations, three-dimensional (3D) metamaterials were developed to yield out-of-plane programmable CTE [14,30,31]. Unfortunately, metamaterials with high thermal-mechanical stability over a broad temperature range are still scarce [32]. It is noteworthy that relying solely on numerical simulation may not provide substantial insights into the underlying physics. Therefore, analytical formulations are sought to predict the equivalent elastic properties of the metamaterial. Addressing this need, Mukhopadhyay and Adhikari [33,34] derived the effective elastic moduli of irregular honeycombs by analyzing the representative unit cells with symmetric boundary conditions. However, as indicated in [35], the lack of high-accurate theoretical models for predicting the thermoelastic behaviors of metamaterials has hindered their development and prospective applications.

Apart from thermal expansion properties, the vibration suppression

performance of mechanical metamaterials should also be considered to meet the practical requirements of many engineering applications [36–38]. The vibration suppression ability of a metamaterial strongly depends on its band gap, within which elastic wave propagation is prohibited [39]. From the formation mechanism, there are two types of band gaps. Bragg scattering (BS) band gaps [40] are formed by the destructive interference of elastic waves scattered by periodic inhomogeneity. Local resonance (LR) band gaps [41] are induced by the out-of-phase motions of local resonators. Numerous efforts have been devoted to generating multiple and/or broadband gaps with different strategies [42–44]. Regarding the theoretical modeling of metamaterials, prevailing techniques include the finite element method (FEM) [45,46], the transfer matrix method (TMM) [47,48], the plane wave expansion (PWE) method [49,50], and the spectral element method (SEM) [51,52]. Among these approaches, SEM has attracted lots of attention because of its superiority in feasibility and efficiency [53]. According to the existing literature, SEM formulations have been well-established for common elements like the regular Timoshenko beam [54] and the Levy-type plate [55]. Recently, Prasad *et al.* [56–58] employed the TMM to analyze wave propagation in periodic curved beams with variable cross-sections. These investigations accounted for the extension effect of the centroid axis of the curved beam, as well as the effects of shear and rotary inertia. However, how to derive the SEM formulation of curved beams, which are standard and common components in many engineering structures, remains to be explored.

Dual- and even multi-functional metamaterials are especially attractive when confronting complex thermal and dynamic loading conditions [59]. Inspired by the rigid unit model [60], some scholars [27,61–63] designed metamaterials with negative Poisson ratios and negative thermal expansion. Lu *et al.* [64] developed a dual-functional metamaterial beam with energy harvesting and vibration control abilities. Besides, several attempts have been made to improve the transmittance proprieties of bending- [65] and stretching-dominated [66] thermal metamaterials. Nevertheless, dual-functional metamaterials featuring zero CTE and broadband vibration suppression ability have not been reported yet [67].

As reviewed above, it can be found that the following questions remain to be answered. (1) Without direct mechanistic relation, can zero CTE and vibration suppression be simultaneously integrated into a metamaterial design? (2) How to construct theoretical formulations of

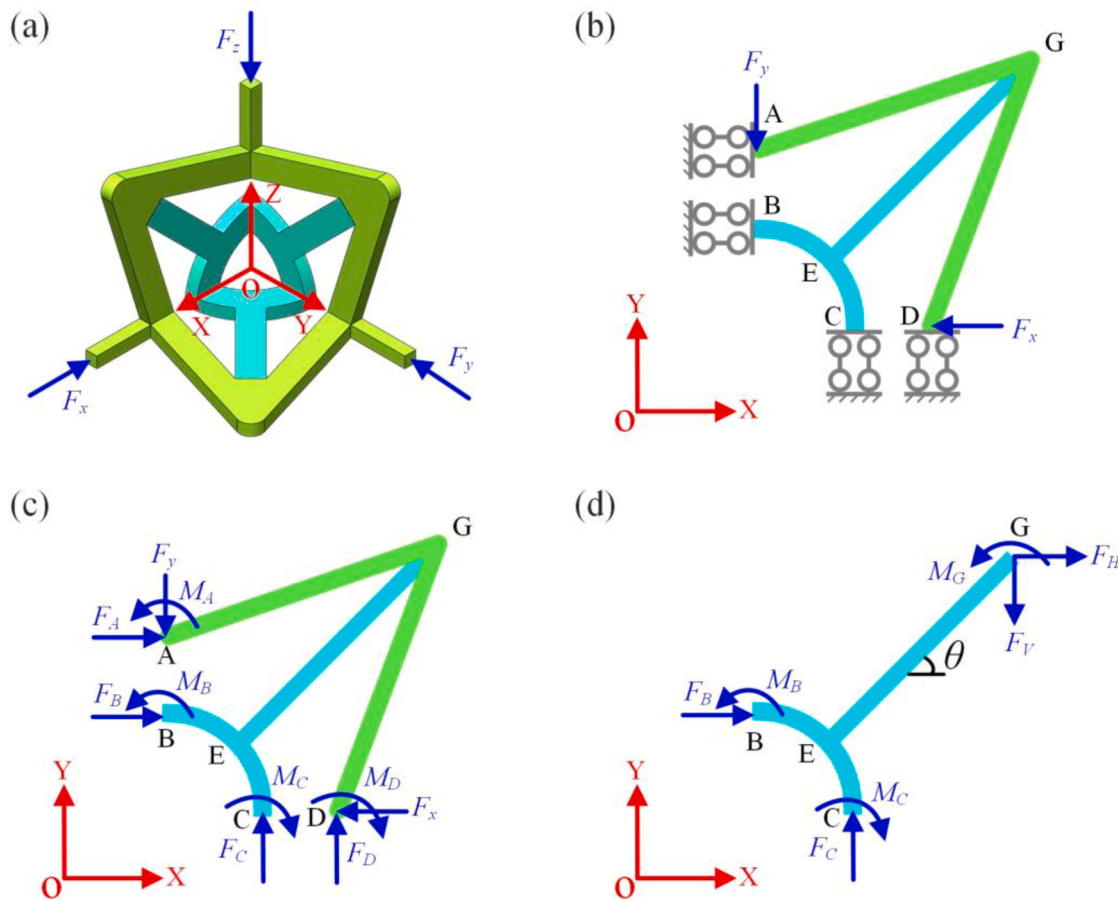


Fig. 2. Symmetrical boundary conditions and free-body diagrams of the components in the metamaterial unit cell. (a) one-eighth of the 3D unit cell under symmetrical boundary conditions; (b) and (c) force diagrams of the in-plane substructure; (d) free-body diagram of the internal substructure. During the thermoelastic deformation, the front, right, and top surfaces of the metamaterial remain flat.

such complicated dual-function metamaterials for guiding their design and optimization? (3) Considering the irregular components of the metamaterial, how to extend the SEM to characterize the dynamic responses of curved beams?

Motivated by the above research gaps, this paper aims to propose a 3D metamaterial with both zero CTE and broadband vibration suppression ability. For this purpose, the coupling deformation and thermal mismatch of bi-materials are introduced into the star-shaped re-entrant structure with rudder-shaped reinforcement struts. The relationships between the geometric parameters and the thermodynamic characteristics are investigated. The desired zero thermal expansion and excellent vibration suppression ability are achieved by tailoring the microstructure.

The rest of the paper is structured as follows. The design strategy and topology configuration of the novel dual-functional metamaterial are first elucidated in [Section 2](#). The thermoelastic model is established in [Section 3](#). The SEM formulation is developed in [Section 4](#). Subsequently, [Section 5](#) presents the feasibility of the proposed methodology and discusses the performance of such dual-functional metamaterials. Finally, [Section 6](#) summarizes the concluding remarks.

2. Geometric configuration of the novel mechanical metamaterial

This section elaborates on the design conception and topology configuration of the dual-functional metamaterial, which is endowed with extraordinary thermal expansion properties and vibration suppression ability.

2.1. Design conception of the novel dual-functional metamaterial

Starting from the fundamental methodologies for achieving zero CTE and vibration suppression, this subsection will propose an integrated design strategy that combines different materials in a meta-structure, leveraging principles of thermal mismatch and wave propagation.

Fundamentally, the primary idea behind zero CTE design is rooted in applying the flexural bending of sub-components to accommodate the overall expansion of the microstructure. Moreover, the vibration suppression design originates from employing locally resonant units to form band gaps. A novel 3D dual-functional metamaterial is designed by incorporating these principles, as illustrated in [Fig. 1](#). In detail, the star-shaped re-entrant lattice is adopted as the exterior structure of the unit cell to change thermomechanical behaviors through thermal expansion incompatibility. To strike a balance between weight and stiffness, rudder-shaped reinforcement struts are introduced into the interior of the unit cell. By incorporating inclined and curved beams, this design will exhibit stretching-dominated modes with bending-dominated behaviors to enhance the mechanical properties.

Additionally, bi-materials are selected to realize simultaneously zero thermal expansion and vibration suppression. The material of the exterior struts (in chartreuse), as depicted in [Fig. 1](#), has a higher CTE. Another material with a lower CTE is selected for the interior struts (in cyan). Through the structural interactions between two constituents, localized rotation and/or bending of particular segments are initiated to enable their thermal expansion to be accommodated within the internal space rather than the external space, thereby achieving the invariance of the overall volume. Furthermore, due to the mechanical impedance

mismatch and the local resonant modes of the inclusions, such composite metamaterial structures tend to form BS and LR band gaps [68].

2.2. Characterization of the novel dual-functional metamaterial

According to the proposed integrated design strategy, this subsection will introduce the topological configuration and geometric characteristics of the novel dual-functional metamaterial in detail.

The geometry of the representative 2D unit cell is determined by six independent variables, i.e., L , R , a , b , t , and θ . As indicated in Fig. 1(a), L is the length of the bevel edge of the internal structure; R is the radius of curved beams; a is the length of the strut connecting to other unit cells; b is the distance from the bottom of the connection strut to the center of the unit cell; θ is the inclined angle of the internal beams; all the beams constituting the unit cell have the same thickness of t . Given the above design parameters, the lengths of the external struts can be calculated by:

$$\begin{cases} L_1 = \left(L + \frac{t}{2} \tan \frac{2\theta + 2\beta - \pi}{4} \right) \frac{\cos \theta}{\sin \beta} \\ L_2 = \left(L + \frac{t}{2} \tan \frac{2\theta + 2\beta - \pi}{4} \right) \frac{-\sin \theta}{\cos(2\theta + \beta)} \end{cases} \quad (1)$$

where the re-entrant angle β of external beams is expressed as

$$\beta = \frac{\pi}{2} - \theta + \arctan \frac{2b\cos\theta - t - ts\sin\theta}{2L - 2bs\sin\theta - t\cos\theta} \quad (2)$$

Fig. 1(b) shows the 3D unit cell configuration, which is obtained by positioning three identical 2D unit cells on three orthogonal planes with their geometric centers coincident. For the sake of central symmetry, all beams are designed with a square cross-section. This proposed unit cell can be tessellated periodically along three coordinate axes to form lattice-based metamaterials. As explained above, the interior inclined struts are expected to conduct stretching-dominated deformation, and the exterior inclined and interior curved beams are more likely to exhibit bending-dominated behavior. Under the combined deformation mode and due to the thermal mismatch, it is feasible for the metamaterial to realize sign-changing CTE. Besides, the periodic arrangement of unit cells naturally gives rise to a metamaterial, implying the possibility of opening band gaps for vibration suppression from the dynamic point of view.

In the following, we demonstrate that combining the bi-material design and the star-shaped re-entrant structure can endow the proposed metamaterial with simultaneous zero thermal expansion and vibration suppression ability.

3. Derivation of the effective CTE

This section will relate the design parameters of the unit cell to a particular thermomechanical response. A theoretical model is developed to reveal the thermoelastic deformation mechanism and quantify the CTE of the proposed metamaterial.

3.1. Elastic deformation analysis

For revealing the deformation behavior of the proposed metamaterial, this subsection will construct a theoretical model that accounts for both stretching and bending deformations, which also serves as a fundamental framework for the subsequent thermoelastic deformation analysis.

Due to the cubic symmetry, taking one-eighth of its 3D unit cell as the representative volume element (RVE) is sufficient in the theoretical analysis. Symmetrical boundary conditions [69] are applied to recover the full 3D unit cell [70].

As illustrated in Fig. 2, three prescribed forces along the three axes are imposed on the RVE, where all boundary nodes are assumed to be at

their respective cross-section centers. As a result of the prescribed boundary conditions, the three rotational degrees of freedom (DOFs) for all endpoints are frozen, and certain translational DOFs are restricted. Hence, all beams can only conduct planar deformation, allowing the 3D problem to be simplified into a 2D one. Taking the X-Y plane of RVE as an example, one can obtain two force balance equations and one moment equilibrium equation by referring to Fig. 2(b) and (c). In addition, the symmetry of the model also indicates that the displacements and deflection angles at the shared connections are zero. Based on Castigliano's second theorem, these boundary conditions are expressed as:

$$\begin{cases} \Delta x_A = \sum_{j=1}^5 \left(\int \frac{F_{ja}}{E_j A_j} \frac{\partial F_{ja}}{\partial F_A} dx_j + \int \frac{\kappa F_{js}}{G_j A_j} \frac{\partial F_{js}}{\partial F_A} dx_j + \int \frac{M_{jj}}{E_j I_j} \frac{\partial M_{jj}}{\partial F_A} dx_j \right) = 0 \\ \Delta \varphi_A = \sum_{j=1}^5 \left(\int \frac{F_{ja}}{E_j A_j} \frac{\partial F_{ja}}{\partial M_A} dx_j + \int \frac{\kappa F_{js}}{G_j A_j} \frac{\partial F_{js}}{\partial M_A} dx_j + \int \frac{M_{jj}}{E_j I_j} \frac{\partial M_{jj}}{\partial M_A} dx_j \right) = 0 \\ \Delta y_D = \sum_{j=1}^5 \left(\int \frac{F_{ja}}{E_j A_j} \frac{\partial F_{ja}}{\partial F_D} dx_j + \int \frac{\kappa F_{js}}{G_j A_j} \frac{\partial F_{js}}{\partial F_D} dx_j + \int \frac{M_{jj}}{E_j I_j} \frac{\partial M_{jj}}{\partial F_D} dx_j \right) = 0 \\ \Delta \varphi_D = \sum_{j=1}^5 \left(\int \frac{F_{ja}}{E_j A_j} \frac{\partial F_{ja}}{\partial M_D} dx_j + \int \frac{\kappa F_{js}}{G_j A_j} \frac{\partial F_{js}}{\partial M_D} dx_j + \int \frac{M_{jj}}{E_j I_j} \frac{\partial M_{jj}}{\partial M_D} dx_j \right) = 0 \\ \Delta \varphi_B = \sum_{j=1}^5 \left(\int \frac{F_{ja}}{E_j A_j} \frac{\partial F_{ja}}{\partial M_B} dx_j + \int \frac{\kappa F_{js}}{G_j A_j} \frac{\partial F_{js}}{\partial M_B} dx_j + \int \frac{M_{jj}}{E_j I_j} \frac{\partial M_{jj}}{\partial M_B} dx_j \right) = 0 \end{cases} \quad (3)$$

where the subscript "j" indicates the strut number (See Appendix A); A_j is the cross-section area; I_j is the second moment of area; κ is the shear correction factor [71]; E_j and G_j denote the elastic modulus and shear modulus, respectively. The internal axial force F_{ja} , the shearing force F_{js} , and the bending moment M_{jj} are detailed in Appendix A.

Substituting the internal force expression of each beam into Eq. (3) yields

$$C_F F = B_F \quad (4)$$

where C_F is a 5×5 coefficient matrix, and B_F denotes the generalized displacement under a single external generalized force $F = [F_A, M_A, F_D, M_D, M_B]^T$.

As formulated above, we can further calculate all reaction forces once unknown generalized forces are solved. Accordingly, the vertical displacement Δy_A at point A and the horizontal displacement Δx_D at point D are calculated by:

$$\begin{cases} \Delta y_A = \sum_{j=1}^5 \left(\int \frac{F_{ja}}{E_j A_j} \frac{\partial F_{ja}}{\partial F_y} dx_j + \int \frac{\kappa F_{js}}{G_j A_j} \frac{\partial F_{js}}{\partial F_y} dx_j + \int \frac{M_{jj}}{E_j I_j} \frac{\partial M_{jj}}{\partial F_y} dx_j \right) \\ \Delta x_D = \sum_{j=1}^5 \left(\int \frac{F_{ja}}{E_j A_j} \frac{\partial F_{ja}}{\partial F_x} dx_j + \int \frac{\kappa F_{js}}{G_j A_j} \frac{\partial F_{js}}{\partial F_x} dx_j + \int \frac{M_{jj}}{E_j I_j} \frac{\partial M_{jj}}{\partial F_x} dx_j \right) \end{cases} \quad (5)$$

The displacements of other endpoints can be obtained likewise. After determining the elastic deformation, it is easy to calculate the effective elastic modulus according to the average stress-strain theorem [62]. Without loss of generality, given the uniaxial compression Δz under the uniform stress σ_z applied in the z -direction, the corresponding effective elastic modulus E_{eff} can be evaluated by:

$$E_{eff} = 2 \frac{(a+b)}{\Delta z} \sigma_z. \quad (6)$$

3.2. Calculation of effective CTE

Based on the formulation of effective elastic modulus, this subsection will quantify the effective CTE of the metamaterial. Moreover, an analytical framework will be developed to achieve zero CTE by

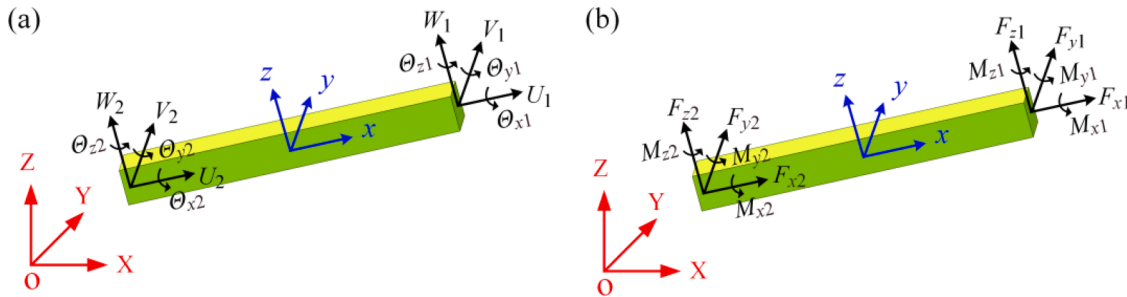


Fig. 3. Spectral element formulation for a straight Timoshenko beam. (a) Boundary displacements and rotations with complete degrees of freedom; (b) Boundary forces and moments at two end nodes. The discrete Fourier transform is conducted to represent all boundary conditions in the frequency domain. The global and local coordinate systems, i.e., X-Y-Z and x-y-z, are adopted for the convenience of variable description.

converting the inverse design problem into a forward search problem.

Given a homogeneous temperature increase ΔT , the thermal expansion problem is investigated to determine the effective CTE of the metamaterial. Since the derivation process resembles that of a purely elastic deformation problem, only the essential modifications are detailed below for the sake of brevity. Apart from the elastic deformation, an axial thermal strain in each strut is also induced by the increase in temperature. Therefore, the axial forces are modified as

$$\hat{F}_{ja} = F_{ja} - E_j A_j \alpha_j \Delta T \quad (7)$$

where α_j is the CTE of strut j . It is worth mentioning that the five force balance equations are still valid in the scenario of thermal deformation. Thus, the shear forces, as given out in [Appendix A](#), remain unchanged.

The effective CTE α of the metamaterial is determined by the ratio of the thermal strain ϵ_t to the temperature increase ΔT . The thermal strain ϵ_t can be evaluated by measuring the thermal deformation relative to the characteristic length, which corresponds to the total strain when external forces are absent. Thus, the effective CTE α of the metamaterial is expressed as:

$$\alpha = \frac{\epsilon_t}{\Delta T} = \frac{\Delta y}{2(a+b)\Delta T} \quad (8)$$

where the vertical thermal deformation Δy can be calculated through [Eqs. \(5\)](#) and [\(7\)](#).

Owing to the cubic symmetry, the effective CTE of the proposed metamaterial is isotropic, i.e. $\alpha = \alpha_x = \alpha_y = \alpha_z$. As formulated above, it can be found that the CTE of the metamaterial depends on the material combination and geometric parameters of the unit cell. This indicates the possibility of tailoring the effective CTE of the metamaterial. We know that most natural materials have positive CTE, and some artificial materials may have negative CTE. A question that naturally arises is: what is the customizability of the proposed metamaterial? In particular, we wonder whether we can achieve zero CTE with such metamaterials for improving dimensional stability.

As formulated above, the CTE of the metamaterial depends on the material combination and geometric parameters of the unit cell. The relationship between these properties is complex, making it challenging to provide a concise closed-form solution for achieving zero CTE. However, utilizing the developed analytical framework, once the material properties and geometric dimensions of the unit cell are known, it becomes straightforward to predict the effective CTE of the metamaterial. This analysis also helps identify which specific geometric parameters play a significant role in effectively reducing the CTE to zero as elaborated in [Section 5.3](#).

From a theoretical perspective, achieving zero CTE is considered an inverse design problem that necessitates a systematical parameter search to find a design solution that meets the specified objective. In essence, the inverse design problem can be transformed into a forward search problem. Given the design space and selected materials, several

available combinations may satisfy the requirement of zero CTE. Note that no direct correlation exists between thermal expansion properties and dynamic characteristics of the metamaterial. Hence, the enumeration method is adopted first to find all possible design combinations to achieve zero CTE. Then, a parametric study will be conducted to explore the structural frequency responses, and attempts will be devoted to improving the vibration suppression characteristics.

4. Dynamic model formulation

In addition to zero CTE, multiple wide band gaps are desired for vibration suppression in engineering structures. This section will formulate the dynamic stiffness matrices (DSMs) of the constituting fundamental elements, i.e., straight and curved beams. The dynamic model of the proposed metamaterial can then be developed by assembling the DSMs of the constituting elements.

4.1. Dynamic stiffness matrix of straight beam

Unlike planar beams, which predominantly concentrate on transverse deflections, the spatial struts in the proposed metamaterial demand a comprehensive analysis encompassing tensile, bending, and torsion deformations. Thus, this subsection is dedicated to extending the standard spectral beam from the 2D scenario to the 3D case.

As shown in [Fig. 3](#), the spectral beam element is characterized by two nodes and twelve DOFs. Combining the discrete Fourier transform with the Timoshenko beam theory, one can recast the in-plane vibration equations into the spectral form [\[43\]](#):

$$\begin{cases} EA \frac{\partial^2 U}{\partial x^2} + \rho A \omega^2 U = 0 \\ \kappa G A \frac{\partial^2 V}{\partial x^2} + \rho A \omega^2 V - \kappa G A \frac{\partial \Theta_z}{\partial x} = 0 \\ \kappa G A \frac{\partial V}{\partial x} + EI_z \frac{\partial^2 \Theta_z}{\partial x^2} + (\rho I_z \omega^2 - \kappa G A) \Theta_z = 0 \end{cases} \quad (9)$$

where ρ and A are the material density and the cross-sectional area of the beam, respectively; I_z is the area moment of inertia around the z -axis. Under the excitation of the angular frequency ω , the amplitudes of axial displacement, transverse displacement, and rotation are denoted as U , V , and Θ_z , respectively.

It can be seen from [Eq. \(9\)](#) that the longitudinal wave propagation is uncoupled with transverse displacement and rotation. Mathematically, the general solutions of [Eq. \(9\)](#) are presented as

$$\begin{cases} U = \chi_1 e^{-ik_0 x} + \chi_2 e^{ik_0 x} \\ V = \chi_3 e^{-ik_1 x} + \chi_4 e^{-ik_2 x} + \chi_5 e^{-ik_3 x} + \chi_6 e^{-ik_4 x} \\ \Theta_z = \chi_1 \alpha_1 e^{-ik_1 x} + \chi_2 \alpha_2 e^{-ik_2 x} + \chi_3 \alpha_3 e^{-ik_3 x} + \chi_4 \alpha_4 e^{-ik_4 x} \end{cases} \quad (10)$$

where i denotes the imaginary unit. By solving the characteristic

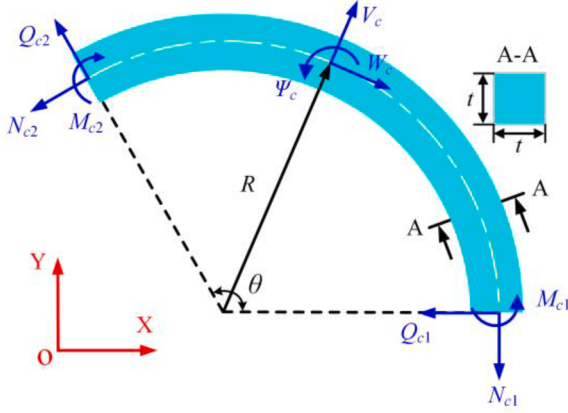


Fig. 4. In-plane vibration of the curved beam. The tangential displacement, radial displacement, and rotational slope of the curved beam are denoted by W_c , V_c , and Ψ_c , respectively. The corresponding tensile force, shearing force, and bending moment are N_c , Q_c , and M_c , respectively.

equations, the wavenumbers k_j ($j=0, 1, \dots, 6$) are given by

$$\left\{ \begin{array}{l} k_0 = \omega \sqrt{\rho/E} \\ k_1 = -k_2 = \sqrt{\left(\frac{I_z}{A} + \frac{EI_z}{\kappa GA}\right) \frac{\rho A \omega^2}{2EI_z} + \omega \sqrt{\frac{\rho A}{EI_z}} \sqrt{\left(1 - \frac{\rho I_z \omega^2}{\kappa GA}\right) + \left(\frac{I_z}{A} + \frac{EI_z}{\kappa GA}\right)^2 \frac{\rho A \omega^2}{4EI_z}}} \\ k_3 = -k_4 = \sqrt{\left(\frac{I_z}{A} + \frac{EI_z}{\kappa GA}\right) \frac{\rho A \omega^2}{2EI_z} - \omega \sqrt{\frac{\rho A}{EI_z}} \sqrt{\left(1 - \frac{\rho I_z \omega^2}{\kappa GA}\right) + \left(\frac{I_z}{A} + \frac{EI_z}{\kappa GA}\right)^2 \frac{\rho A \omega^2}{4EI_z}}} \end{array} \right. \quad (11)$$

Moreover, the coefficients of general solutions satisfy the following relationships:

$$a_j = -i \frac{\kappa G k_j^2 - \rho \omega^2}{\kappa G k_j} \quad (12)$$

For the two-node spectral beam element in the local reference frame, the boundary conditions of displace and force are imposed:

$$\left\{ \begin{array}{l} U_1 = U|_{x=0}, U_2 = U|_{x=l} \\ V_1 = V|_{x=0}, V_2 = V|_{x=l} \\ \Theta_{z1} = \Theta_z|_{x=0}, \Theta_{z2} = \Theta_z|_{x=l} \end{array} \right. \text{ and } \left\{ \begin{array}{l} F_{x1} = F_x|_{x=0}, F_{x2} = F_x|_{x=l} \\ F_{y1} = F_y|_{x=0}, F_{y2} = F_y|_{x=l} \\ M_{z1} = M_z|_{x=0}, M_{z2} = M_z|_{x=l} \end{array} \right. \quad (13)$$

where l is the distance between the two boundary nodes. The internal bending moment and shear force of the straight beam element take the following forms:

$$M_z = EI_z \frac{\partial \Theta_z}{\partial x}, F_y = \kappa GA \left(\frac{\partial V}{\partial x} - \Theta_z \right). \quad (14)$$

By substituting Eq. (10) into (13), the relationship between the nodal displacement vector $\mathbf{d}_v = [U_1, V_1, \Theta_{z1}, U_2, V_2, \Theta_{z2}]^T$ and the coefficient vector $\mathbf{b}_v = [\chi_1, \chi_3, \chi_4, \chi_2, \chi_5, \chi_6]^T$ can be recast into the linear matrix form:

$$\mathbf{d}_v = \mathbf{H}_v \mathbf{b}_v \quad (15)$$

where the matrix \mathbf{H}_v is:

$$\mathbf{H}_v = \begin{bmatrix} 1 & 0 & 0 & 1 & 0 & 0 \\ 0 & 1 & 1 & 0 & 1 & 1 \\ 0 & \alpha_1 & \alpha_2 & 0 & \alpha_3 & \alpha_4 \\ e^{-ik_0 l} & 0 & 0 & e^{ik_0 l} & 0 & 0 \\ 0 & e^{-ik_1 l} & e^{-ik_2 l} & 0 & e^{-ik_3 l} & e^{-ik_4 l} \\ 0 & \alpha_1 e^{-ik_1 l} & \alpha_2 e^{-ik_2 l} & 0 & \alpha_3 e^{-ik_3 l} & \alpha_4 e^{-ik_4 l} \end{bmatrix} \quad (16)$$

In addition, the nodal force vector $\mathbf{F}_v = [F_{x1}, F_{y1}, M_{z1}, F_{x2}, F_{y2}, M_{z2}]^T$ is associated with the coefficient vector \mathbf{b}_v , and we have

$$\mathbf{F}_v = [\mathbf{R}_1 \quad \mathbf{R}_2] \mathbf{b}_v = [\mathbf{R}_1 \quad \mathbf{R}_2] \mathbf{H}_v^{-1} \mathbf{d}_v \quad (17)$$

where the block matrices \mathbf{R}_1 and \mathbf{R}_2 are derived as:

$$\left\{ \begin{array}{l} \mathbf{R}_1 = \begin{bmatrix} iEAk_0 & 0 & 0 \\ 0 & -\kappa GA(-ik_1 - \alpha_1) & -\kappa GA(-ik_2 - \alpha_2) \\ 0 & iEI_z \alpha_1 k_1 & iEI_z \alpha_2 k_2 \\ -iEAk_0 e^{-ik_0 l} & 0 & 0 \\ 0 & \kappa GA(-ik_1 - \alpha_1) e^{-ik_1 l} & \kappa GA(-ik_2 - \alpha_2) e^{-ik_2 l} \\ 0 & -iEI_z \alpha_1 k_1 e^{-ik_1 l} & -iEI_z \alpha_2 k_2 e^{-ik_2 l} \end{bmatrix} \\ \mathbf{R}_2 = \begin{bmatrix} -iEAk_0 & 0 & 0 \\ 0 & -\kappa GA(-ik_3 - \alpha_3) & -\kappa GA(-ik_4 - \alpha_4) \\ 0 & iEI_z \alpha_3 k_3 & iEI_z \alpha_4 k_4 \\ iEAk_0 e^{-ik_0 l} & 0 & 0 \\ 0 & \kappa GA(-ik_3 - \alpha_3) e^{-ik_3 l} & \kappa GA(-ik_4 - \alpha_4) e^{-ik_4 l} \\ 0 & -iEI_z \alpha_3 k_3 e^{-ik_3 l} & -iEI_z \alpha_4 k_4 e^{-ik_4 l} \end{bmatrix} \end{array} \right. \quad (18)$$

Therefore, the DSM (\mathbf{S}_v) for the in-plane vibration of the beam element can be calculated by:

$$\mathbf{S}_v = [\mathbf{R}_1 \quad \mathbf{R}_2] \mathbf{H}_v^{-1}. \quad (19)$$

By taking advantage of the cross-section symmetry, we can quickly set up the DSM for the vibration in the x - z plane from Eq. (19). Besides, the spectral formulation of the torsional motion is similar to that of the

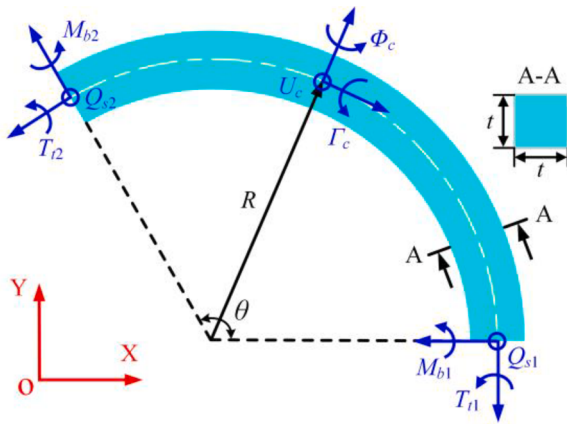


Fig. 5. Out-of-plane vibration of the curved beam. The transverse deflection, bending rotation, and twist angle are denoted by U_c , Φ_c , and Γ_c , respectively. The corresponding shearing force, tensile moment, and bending moment are Q_s , T_t , and M_b , respectively.

Table 1
Geometric parameters of the metamaterial.

Structural parameters	Design values
Radius of the curved beams R	15.00 mm
Length of the interior oblique struts L	45.00 mm
Half-width of the interior lattice b	25.00 mm
Length of the exterior vertical beams a	20.00 mm
Thickness of all beams t	4.00 mm
Inclined angle of the interior beams θ	45.00°

Table 2
Exterior and interior material properties of the metamaterial.

Material	Poisson ratio	Elastic modulus (GPa)	CTE (ppm/°C)	Density (kg/m³)
Steel	0.30	200	12.0	7850
Invar alloy	0.29	144	1.2	8050

axial displacement. The details, which can be found in Refs [43,52], are not repeated here for brevity. By assembling the DSMs for different direction vibrations, the spectral formulation for the 3D straight beam is formulated as:

$$\mathbf{F}_b = \mathbf{S}_b(\omega)\mathbf{d}_b \quad (20)$$

where \mathbf{S}_b is the full DSM of the straight beam element, and the vectors of nodal force and displacement, i.e., \mathbf{F}_b and \mathbf{d}_b , incorporate all the tensile, bending, and torsion components.

4.2. Dynamic stiffness matrix of curved beam

Due to the curved nature, the tangential displacement of a curved beam is coupled with its rotation and radial displacement. Therefore, compared with the spectral element formulation of straight beams, the DSM derivation of curved beams is more challenging. This subsection will present the formulation of the DSM of curved beams.

4.2.1. In-plane vibration

It is well-known that the vibration features of curved beams can be comprehensively characterized by in-plane and out-of-plane modes. In this subsection, our efforts will be dedicated to deriving the dynamic stiffness formulations of the in-plane vibration.

As depicted in Fig. 4, a circular curved beam can be characterized by

its radius R at the neutral axis, the thickness t , and the radian θ . For description, we introduce the following dimensionless parameters:

$$\begin{aligned} \eta_{c1} &= \frac{t}{2R} \coth\left(\frac{t}{2R}\right) - 1, \eta_{c2} = \eta_{c1}(\eta_{c1} + 1) + \frac{t^2}{12R^2}, \eta_{c3} \\ &= \eta_{c1} \left(\eta_{c1}^2 + \eta_{c1} + \frac{t^2}{4R^2} \right) + \frac{t^2}{12R^2} \end{aligned} \quad (21)$$

Considering the coupling influence of shear deformation and rotary inertia, the Timoshenko beam theory is applied to analyze the vibration response of curved beams. As formulated in [72], the in-plane vibration of the curved beam is governed by:

$$\begin{cases} \frac{\partial Q_c}{\partial \theta} + N_c + \omega^2 \rho_c A_c R (1 + \eta_{c1}) V_c = 0 \\ \frac{\partial M_c}{R \partial \theta} + Q_c + \omega^2 \rho_c A_c R (\eta_{c2} W_c + \eta_{c3} R \psi_c) V_c = 0 \\ \frac{\partial N_c}{\partial \theta} - Q_c + \omega^2 \rho_c A_c R [(1 + \eta_{c1}) W_c + \eta_{c2} R \psi_c] = 0 \end{cases} \quad (22)$$

where ω is the angular vibration frequency, and the variables with the subscript “c” correspond to the physical parameters of curved beams. More specifically, the tensile force N_c , shearing force Q_c , and bending moment M_c are expressed as

$$N_c = \frac{E_c A_c}{R} \left(\frac{\partial W_c}{\partial \theta} - V_c \right), Q_c = \kappa_c A_c G_c \left(\frac{\partial V_c}{R \partial \theta} + \frac{W_c}{R} - \psi_c \right), M_c = \eta_{c1} E_c A_c R \frac{\partial \psi_c}{\partial \theta} \quad (23)$$

After substituting Eq. (23) into Eq. (22), one can obtain

$$\begin{cases} \frac{\kappa_c}{2(1+\nu)} V'_c - \left(1 - \lambda_c \frac{1+\eta_{c1}}{s_y} \right) V_c + \left[1 + \frac{\kappa_c}{2(1+\nu)} \right] W'_c - \frac{\kappa_c}{2(1+\nu)} \psi'_c = 0 \\ \frac{\kappa_c}{2(1+\nu)} V'_c + \left[\frac{\kappa_c}{2(1+\nu)} + \lambda_c \frac{\eta_{c2}}{s_y} \right] W_c + \eta_{c1} \psi''_c - \left[\frac{\kappa_c}{2(1+\nu)} - \lambda_c \frac{\eta_{c3}}{s_y} \right] \psi'_c = 0 \\ \left[1 + \frac{\kappa_c}{2(1+\nu)} \right] V'_c - W''_c + \left[\frac{\kappa_c}{2(1+\nu)} - \lambda_c \frac{1+\eta_{c1}}{s_y} \right] W_c - \left[\frac{\kappa_c}{2(1+\nu)} + \lambda_c \frac{\eta_{c2}}{s_y} \right] \psi'_c = 0 \end{cases} \quad (24)$$

where ν is the Poisson ratio. The frequency parameter λ_c and the slenderness ratio s_y are defined as

$$\lambda_c = \frac{\omega^2 \rho_c A_c R^4}{E_c I_y}, s_y = \frac{A_c R^2}{I_y}, \quad (25)$$

with I_y denoting the cross-sectional inertia moment around the y -axis. For the convenience of illustration, we further introduce the following dimensionless parameters:

$$\begin{cases} u = \frac{V_c}{R}, w = \frac{W_c}{R}, \psi = \frac{\psi_c}{R}, \\ N = \frac{N_c}{E_c A_c}, Q_x = \frac{Q_c}{E_c A_c}, M_y = \frac{M_c}{E_c A_c R} \end{cases} \quad (26)$$

Accordingly, the transfer matrix C_{in} that relates the general displacement vector $\mathbf{U}_{in} = [u \ w \ \psi \ u' \ w' \ \psi']^T$ and the general force vector $\mathbf{F}_{in} = [N \ Q_x \ M_y]^T$ can be determined from Eq. (23) as below:

$$\mathbf{F}_{in} = \begin{bmatrix} -1 & 0 & 0 & 0 & 1 & 0 \\ 0 & \frac{\kappa_c}{2(1+\nu)} & -\kappa_c & \frac{\kappa_c}{2(1+\nu)} & 0 & 0 \\ 0 & 0 & 0 & 0 & 0 & \eta_{c1} \end{bmatrix} \mathbf{U}_{in} = \mathbf{C}_{in} \mathbf{U}_{in} \quad (27)$$

Mathematically, the general solutions of the in-plane vibration for the curve beam element take the spectral form of:

$$u(\theta) = \alpha_{in} e^{-ip\theta}, w(\theta) = \beta_{in} e^{-ip\theta}, \psi(\theta) = \gamma_{in} e^{-ip\theta} \quad (28)$$

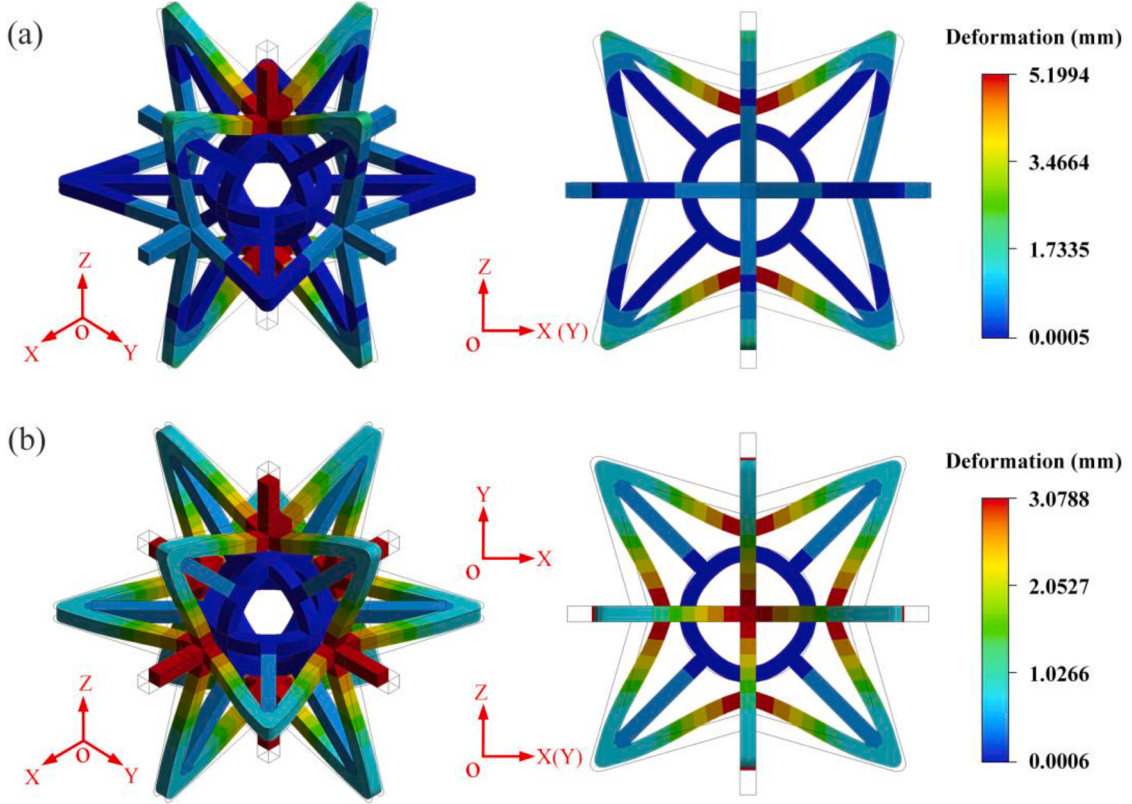


Fig. 6. Elastic deformation of the metamaterial unit cell. (a) Axial compression along the z direction under the uniform stress of 2000 MPa; (b) Multiaxial compression along the three orthogonal directions with each cross-section subjected to 2000 MPa. The gray and colored lines denote the undeformed and deformed configurations, respectively.

where p is the wavenumber. Combining Eqs.(28) and (24) yields an eigenvalue problem:

$$u = \mathbf{e}_u \boldsymbol{\alpha}, w = \mathbf{e}_u \text{diag}(\boldsymbol{\beta}) \boldsymbol{\alpha}, \psi = \mathbf{e}_u \text{diag}(\boldsymbol{\gamma}) \boldsymbol{\alpha} \quad (31)$$

where $\text{diag}(\cdot)$ is the diagonal operator. The corresponding vectors are detailed as

$$\begin{bmatrix} \frac{\kappa_c}{2(1+\nu)} p^2 - \lambda_c \frac{1 + \eta_{c1}}{s_y} + 1 & ip \left[1 + \frac{\kappa_c}{2(1+\nu)} \right] & -ip \frac{\kappa_c}{2(1+\nu)} \\ ip \frac{\kappa_c}{2(1+\nu)} & \frac{\kappa_c}{2(1+\nu)} - \lambda_c \frac{\eta_{c2}}{s_y} & \eta_{c1} p^2 + \frac{\kappa_c}{2(1+\nu)} - \lambda_c \frac{\eta_{c3}}{s_y} \\ ip \left[1 + \frac{\kappa_c}{2(1+\nu)} \right] & \lambda_c \frac{1 + \eta_{c1}}{s_y} - p^2 - \frac{\kappa}{2(1+\nu)} & \frac{\kappa_c}{2(1+\nu)} + \lambda_c \frac{\eta_{c2}}{s_y} \end{bmatrix} \begin{bmatrix} \alpha_{in} \\ \beta_{in} \\ \gamma_{in} \end{bmatrix} = \begin{bmatrix} 0 \\ 0 \\ 0 \end{bmatrix} \quad (29)$$

It is known that nontrivial solutions exist in homogeneous linear equations only if the matrix determinant is zero. According to Eq. (29), the dispersion relation for the in-plane vibration can be obtained as

$$c_{in,1} p^6 + c_{in,2} p^4 + c_{in,3} p^2 + c_{in,4} = 0 \quad (30)$$

which indicates that there exist six wavenumbers p_1, p_2, \dots, p_6 . After solving the numerical roots of Eq. (30), one can further calculate $\alpha_{in,i}$, $\beta_{in,i}$ and $\gamma_{in,i}$ for each wavenumber p_i ($i=1, 2, \dots, 6$) from Eq. (29).

Consequently, the general solutions of the in-plane vibration are recast into the linear algebraic form as below:

$$\begin{cases} \mathbf{e}_u = [e_1 \ e_2 \ e_3 \ e_4 \ e_5 \ e_6], e_j = e^{-ip_j \theta} \\ \boldsymbol{\alpha} = [\alpha_{in,1} \ \alpha_{in,2} \ \alpha_{in,3} \ \alpha_{in,4} \ \alpha_{in,5} \ \alpha_{in,6}]^T \\ \boldsymbol{\beta} = [\beta_1 \ \beta_2 \ \beta_3 \ \beta_4 \ \beta_5 \ \beta_6]^T \\ \boldsymbol{\gamma} = [\gamma_1 \ \gamma_2 \ \gamma_3 \ \gamma_4 \ \gamma_5 \ \gamma_6]^T \end{cases} \quad (32)$$

where the scaled parameters β_j and γ_j ($j=1, 2, \dots, 6$) are given by

$$\beta_j = \beta_{in,j} / \alpha_{in,j}, \gamma_j = \gamma_{in,j} / \alpha_{in,j} \quad (33)$$

The nodal forces and the displacements at the two ends of the curved

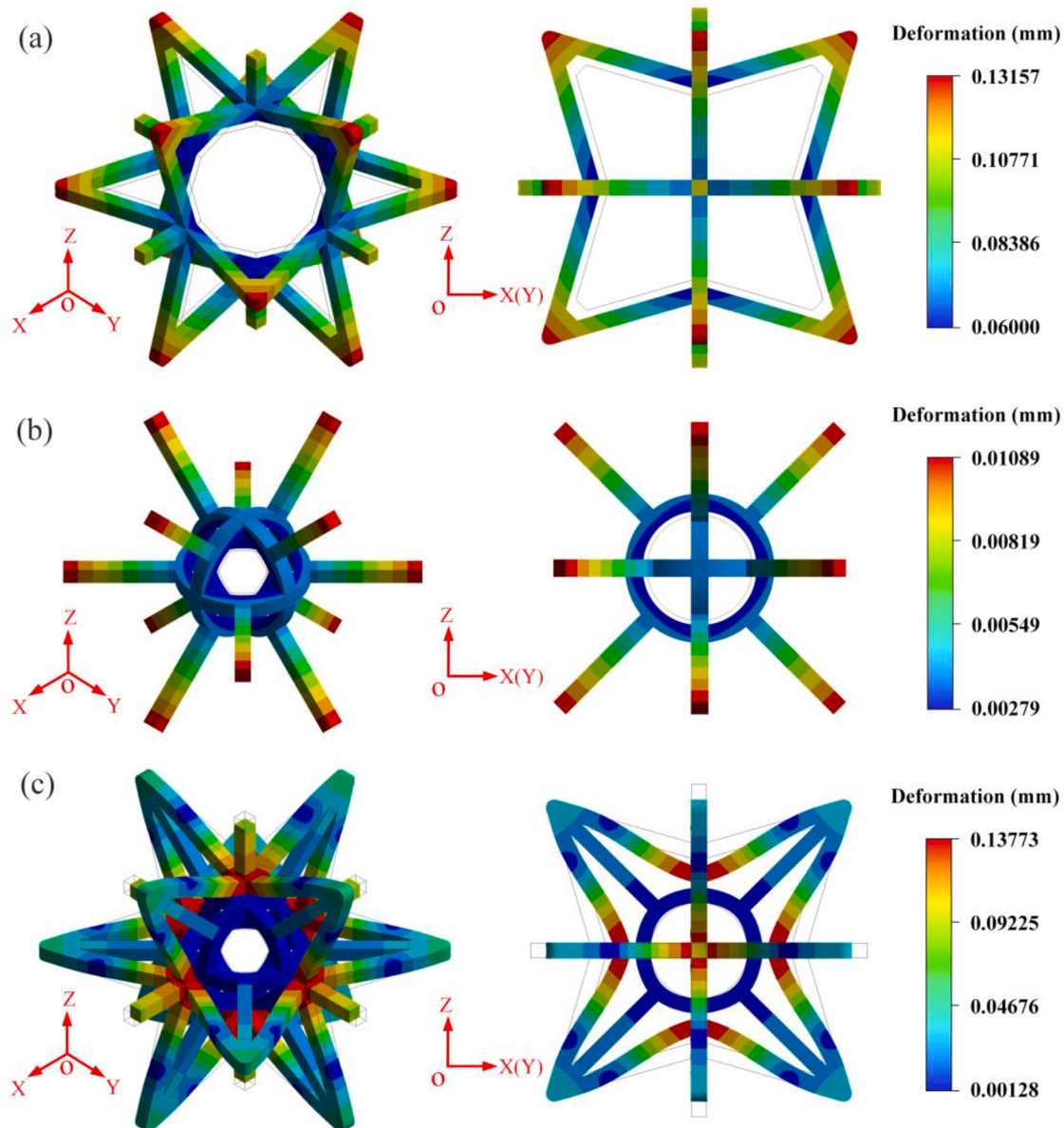


Fig. 7. Thermal deformation of the unit with thermal mismatch effect in response to a temperature increase. (a) and (b) depict the thermal expansion of the independent exterior and interior substructures, respectively. (c) shows the thermal deformation of the entire metamaterial unit. The gray lines denote the undeformed configuration, and the colored lines represent the deformed configuration. The metamaterial of cubic symmetry possesses isotropic thermomechanical properties. The metamaterial with prescribed parameters exhibits a negative CTE due to the thermal mismatch and re-entrant unfolding mechanisms.

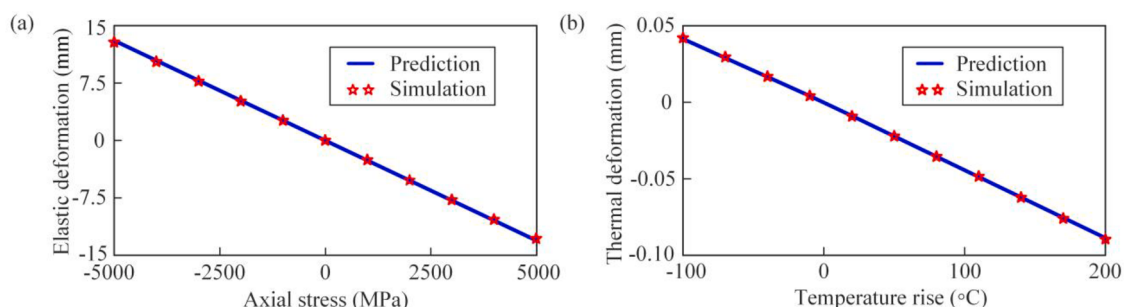


Fig. 8. Elastic and thermal deformations in different loading scenarios. (a) Multiaxial tensile and compression; (b) thermal expansion and contraction over a wide temperature change. The theoretical predictions are well consistent with the simulation results. These case studies show that the metamaterial exhibits linear thermoelasticity.

Table 3

Effective CTE and elastic modulus of the metamaterial with Steel-Invar.

Results	Elastic modulus (GPa)	CTE (ppm/°C)
Theoretical prediction	17.0952	-9.8557
FE simulation	17.3098	-9.9405
Relative error	-1.24%	-0.86%

beam are concentrated into the vectors \mathbf{f}_{in} and \mathbf{d}_{in} :

$$\begin{cases} \mathbf{f}_{in} = [N(0) \ Q(0) \ M(0) \ N(\theta) \ Q(\theta) \ M(\theta)]^T = [N_1 \ Q_1 \ M_1 \ N_2 \ Q_2 \ M_2]^T, \\ \mathbf{d}_{in} = [u(0) \ w(0) \ \psi(0) \ u(\theta) \ w(\theta) \ \psi(\theta)]^T = [u_1 \ w_1 \ \psi_1 \ u_2 \ w_2 \ \psi_2]^T. \end{cases} \quad (34)$$

According to Eq. (31), we obtain the following relationship:

$$\mathbf{d}_{in} = \begin{bmatrix} 1 & 1 & 1 & 1 & 1 & 1 \\ \beta_1 & \beta_2 & \beta_3 & \beta_4 & \beta_5 & \beta_6 \\ \gamma_1 & \gamma_2 & \gamma_3 & \gamma_4 & \gamma_5 & \gamma_6 \\ e_1 & e_2 & e_3 & e_4 & e_5 & e_6 \\ \beta_1 e_1 & \beta_2 e_2 & \beta_3 e_3 & \beta_4 e_4 & \beta_5 e_5 & \beta_6 e_6 \\ \gamma_1 e_1 & \gamma_2 e_2 & \gamma_3 e_3 & \gamma_4 e_4 & \gamma_5 e_5 & \gamma_6 e_6 \end{bmatrix} \boldsymbol{\alpha} = \mathbf{H}_{in} \boldsymbol{\alpha} \quad (35)$$

Combining Eqs.(31) and (35), one can obtain

$$u = \mathbf{e}_u \mathbf{H}_{in}^{-1} \mathbf{d}_{in}, w = \mathbf{e}_w \text{diag}(\boldsymbol{\beta}) \mathbf{H}_{in}^{-1} \mathbf{d}_{in}, \psi = \mathbf{e}_\psi \text{diag}(\boldsymbol{\gamma}) \mathbf{H}_{in}^{-1} \mathbf{d}_{in} \quad (36)$$

On this basis, substituting Eq. (36) into Eq. (27) yields the mapping relation from \mathbf{d}_{in} to \mathbf{f}_{in} , which is expressed as

$$\mathbf{f}_{in} = \begin{bmatrix} \mathbf{C}_{in} & \mathbf{0} \\ \mathbf{0} & \mathbf{C}_{in} \end{bmatrix} \mathbf{R}_{in} \mathbf{H}_{in}^{-1} \mathbf{d}_{in} = \mathbf{S}_{in} \mathbf{d}_{in} \quad (37)$$

where \mathbf{S}_{in} is the DSM of the in-plane vibration of the curved beam, and the matrix \mathbf{R}_{in} is derived as:

$$\mathbf{R}_{in} = \begin{bmatrix} 1 \ \beta_1 \ \gamma_1 - ip_1 \ \beta_1 - ip_1 \gamma_1 \ e_1 \ \beta_1 e_1 \ \gamma_1 e_1 - ip_1 e_1 - ip_1 \beta_1 e_1 - ip_1 \gamma_1 e_1 \\ 1 \ \beta_2 \ \gamma_2 - ip_2 \ \beta_2 - ip_2 \gamma_2 \ e_2 \ \beta_2 e_2 \ \gamma_2 e_2 - ip_2 e_2 - ip_2 \beta_2 e_2 - ip_2 \gamma_2 e_2 \\ 1 \ \beta_3 \ \gamma_3 - ip_3 \ \beta_3 - ip_3 \gamma_3 \ e_3 \ \beta_3 e_3 \ \gamma_3 e_3 - ip_3 e_3 - ip_3 \beta_3 e_3 - ip_3 \gamma_3 e_3 \\ 1 \ \beta_4 \ \gamma_4 - ip_4 \ \beta_4 - ip_4 \gamma_4 \ e_4 \ \beta_4 e_4 \ \gamma_4 e_4 - ip_4 e_4 - ip_4 \beta_4 e_4 - ip_4 \gamma_4 e_4 \\ 1 \ \beta_5 \ \gamma_5 - ip_5 \ \beta_5 - ip_5 \gamma_5 \ e_5 \ \beta_5 e_5 \ \gamma_5 e_5 - ip_5 e_5 - ip_5 \beta_5 e_5 - ip_5 \gamma_5 e_5 \\ 1 \ \beta_6 \ \gamma_6 - ip_6 \ \beta_6 - ip_6 \gamma_6 \ e_6 \ \beta_6 e_6 \ \gamma_6 e_6 - ip_6 e_6 - ip_6 \beta_6 e_6 - ip_6 \gamma_6 e_6 \end{bmatrix}^T \quad (38)$$

4.2.2. Out-of-plane vibration

After the DSM of the in-plane vibration is derived, this subsection will further develop the dynamic stiffness formulation for the out-of-plane vibration of the curved beam.

The governing equations for the out-of-plane vibration of the curved Timoshenko beam, as illustrated in Fig. 5, are represented as

$$\left\{ \begin{array}{l} \frac{\partial T_t}{R\partial\theta} + \frac{M_b}{R} + \rho_c J_z \omega^2 \Gamma_c = 0 \\ -\frac{\partial M_b}{R\partial\theta} + \frac{T_t}{R} - Q_s + \rho_c I_x \omega^2 \Phi_c = 0 \\ \frac{\partial Q_s}{R\partial\theta} + \rho_c A_c \omega^2 U_c = 0 \end{array} \right. \quad (39)$$

where I_x is the cross-section inertia moment around the x -axis, and J_z is the polar inertia moment. The bending moment M_b , shearing force Q_s , and torsional moment T_t are given by:

$$M_b = \frac{E_c I_x}{R} \left(-\Gamma_c - \frac{\partial \Phi_c}{\partial \theta} \right), Q_s = \kappa_c G A \left(\Phi_c + \frac{\partial U_c}{R\partial\theta} \right), T_t = \frac{G C_z}{R} \left(-\Phi_c + \frac{\partial \Gamma_c}{\partial \theta} \right), \quad (40)$$

where C_z is the torsional inertia moment.

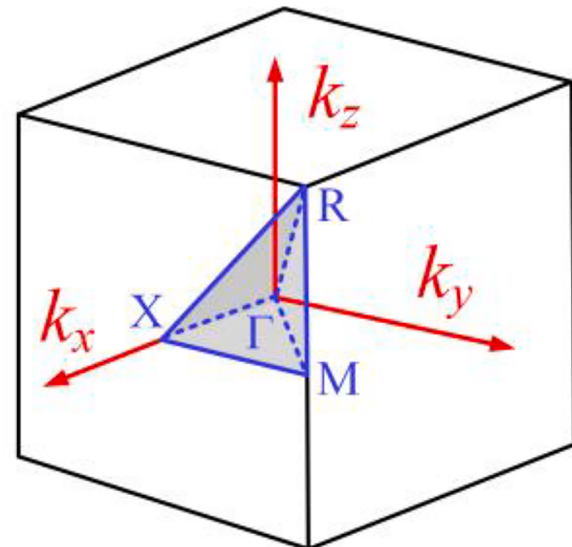


Fig. 10. Irreducible Brillouin zone (the gray area) of the metamaterial. k_x , k_y and k_z are the components of the wave vector in three directions. Along the boundary path, the varying curve of the eigenfrequency with wave vector k can be obtained, i.e., the band structure of the metamaterial.

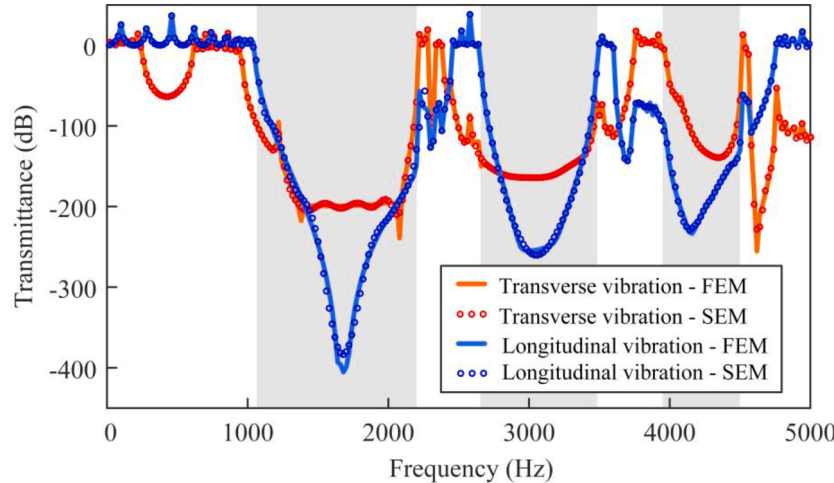


Fig. 9. Transmittance analysis on the transverse and longitudinal vibrations for the metamaterial via SEM and FEM. Three apparent vibration attenuation valleys exist on the transmittance response over the frequency ranges of 1036.50–2217.57 Hz, 2633.99–3497.31 Hz, and 3942.71–4517.63 Hz, respectively.

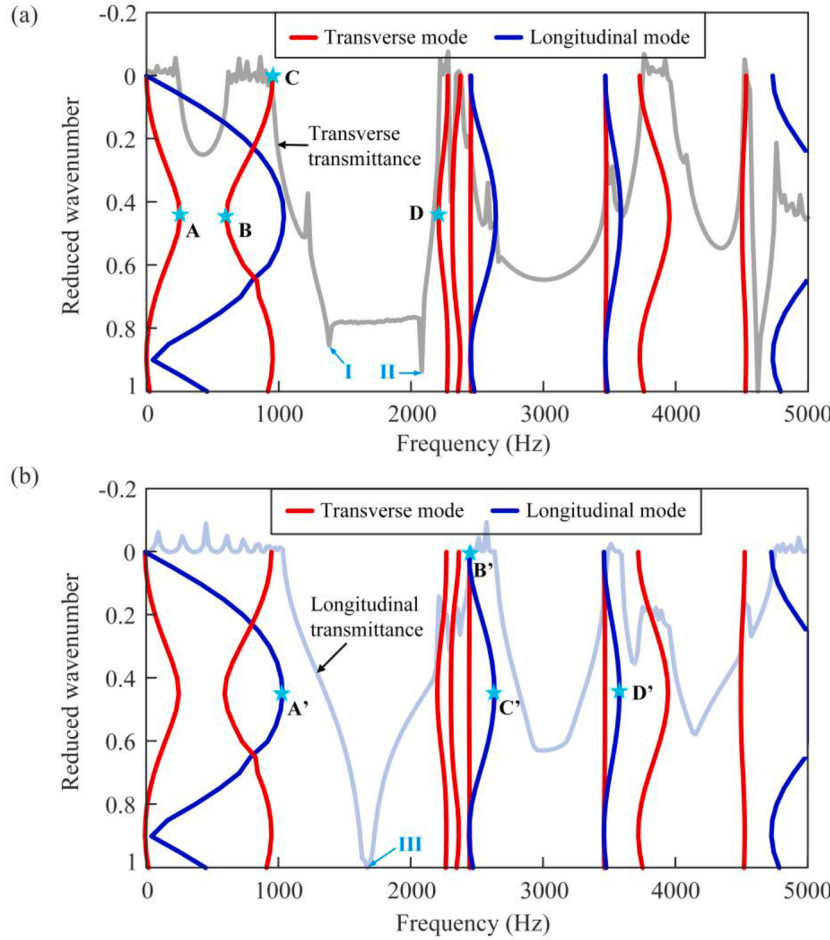


Fig. 11. Band structure of the metamaterial. The dispersion curves in red and blue correspond to the transverse and longitudinal modes, respectively. (a) The transverse transmittance curve of the metamaterial comprising 10 unit cells is appended for comparison. The amplitude is unit-normalized. The vibration attenuation valleys appear in between those red curves. A, B, C, and D are located at the bounds of transverse band gaps, and their corresponding frequencies are 254.41 Hz, 600.89 Hz, and 2217.57 Hz, respectively. (b) The longitudinal transmittance curve is appended for comparison. The amplitude is unit-normalized. The vibration attenuation valleys form in between those blue curves. A', B', C', and D' are located at the longitudinal band gap bounds, with frequencies of 1036.50 Hz, 2452.68 Hz, 2633.99 Hz, and 3584.64 Hz, respectively.

Substituting Eq. (40) into Eq. (39) yields

$$\left\{ \begin{array}{l} \mu\Gamma_c^{''} - \left[I - \lambda_x \left(s_x^{-1} + s_y^{-1} \right) \right] \Gamma_c - (I + \mu)\Phi_c^{'} = 0 \\ -\kappa_c \frac{G}{E} s_x U_c^{'} + (I + \mu)\Gamma_c^{'} + \Phi_c^{''} - \left(\mu + \kappa_c \frac{G}{E} s_x - \frac{\lambda_x}{s_x} \right) \Phi_c = 0 \\ \kappa_c \frac{G}{E} s_x U_c^{''} + \lambda_x U_c + \kappa_c \frac{G}{E} s_x \Phi_c^{'} = 0 \end{array} \right. \quad (41)$$

where the intermediate variables are defined as:

$$\lambda_x = \frac{\omega^2 \rho_c A_c R^4}{E_c I_x}, \mu = \frac{G C_z}{E_c I_x}, s_x = \frac{A_c R^2}{I_x} \quad (42)$$

In addition, the following dimensionless parameters are introduced to simplify the formulation:

$$M_x = \frac{R M_c}{E_c I_x}, Q_y = \frac{R^2 Q_s}{E_c I_x}, T = \frac{R T_t}{E_c I_x} \quad (43)$$

Given that $\mathbf{U}_{out} = [\Phi_b \ U_t \ \Gamma_t \ \Phi_b^{'} \ U_t^{'} \ \Gamma_t^{'}]^T$ and $\mathbf{F}_{out} = [M_x \ Q_y \ T]^T$, we have

$$\mathbf{F}_{out} = \begin{bmatrix} 0 & 0 & -1 & -1 & 0 & 0 \\ \kappa_c \frac{G}{E_c} s_x & 0 & 0 & 0 & \kappa_c \frac{G}{E_c} s_x & 0 \\ -\mu & 0 & 0 & 0 & 0 & \mu \end{bmatrix} \mathbf{U}_{out} = \mathbf{C}_{out} \mathbf{U}_{out} \quad (44)$$

Following the spectral analysis procedures, the general solutions of Eq. (41) are assumed to be

$$\Phi_c(\theta) = \alpha_{out} e^{-iq\theta}, U_c(\theta) = \beta_{out} e^{-iq\theta}, \Gamma_c(\theta) = \gamma_{out} e^{-iq\theta} \quad (45)$$

where q is the wavenumber. Substituting Eq. (45) into Eq. (41) yields

$$\begin{bmatrix} iq(1+\mu) & 0 & \lambda_x \left(s_x^{-1} + s_y^{-1} \right) - q^2 \mu - 1 \\ \lambda_x s_x^{-1} - q^2 - \mu - \kappa_c \frac{G}{E_c} s_x & iq \kappa_c \frac{G}{E_c} s_x & -iq(1+\mu) \\ -iq \kappa_c \frac{G}{E_c} s_x & \lambda_x - q^2 \kappa_c \frac{G}{E_c} s_x & 0 \end{bmatrix} \begin{bmatrix} \alpha_{out} \\ \beta_{out} \\ \gamma_{out} \end{bmatrix} = \begin{bmatrix} 0 \\ 0 \\ 0 \end{bmatrix} \quad (46)$$

The existence condition of nontrivial solutions gives the sixth-order dispersion relation as

$$c_{out,1} p^6 + c_{out,2} p^4 + c_{out,3} p^2 + c_{out,4} = 0 \quad (47)$$

From Eqs. (46) and (47), $\alpha_{out,j}$, $\beta_{out,j}$ and $\gamma_{out,j}$ can be fully determined for each wavenumber q_j ($j=1, 2, \dots, 6$). On this basis, similar to the derivation of H_{in} and R_{in} , obtaining the transfer matrices H_{out} and R_{out} for the out-of-plane vibration becomes easy. For brevity, the expressions of H_{out} and R_{out} are not repeated here. Finally, the DSM for the out-of-plane vibration (S_{out}) can be formulated as

$$\mathbf{f}_{out} = \begin{bmatrix} \mathbf{C}_{out} & \mathbf{0} \\ \mathbf{0} & \mathbf{C}_{out} \end{bmatrix} \mathbf{R}_{out} \mathbf{H}^{-1} \mathbf{d}_{out} = \mathbf{S}_{out} \mathbf{d}_{out} \quad (48)$$

where the nodal forces (\mathbf{f}_{out}) and the general displacements (\mathbf{d}_{out}) at the two ends are defined as:

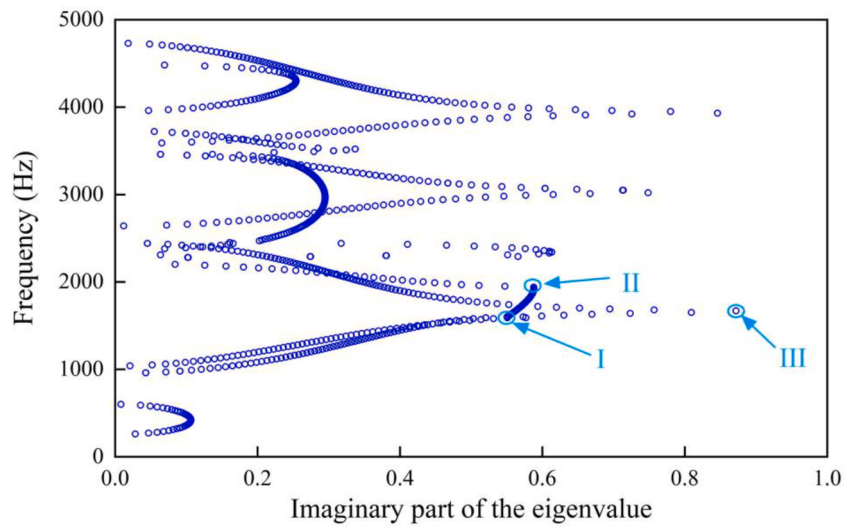


Fig. 12. Imaginary part of the band structure for the metamaterial. Annotations I and II are located at the transverse transmittance curve as shown in Fig. 11(a), while III is positioned at the longitudinal transmittance curve as depicted in Fig. 11(b).

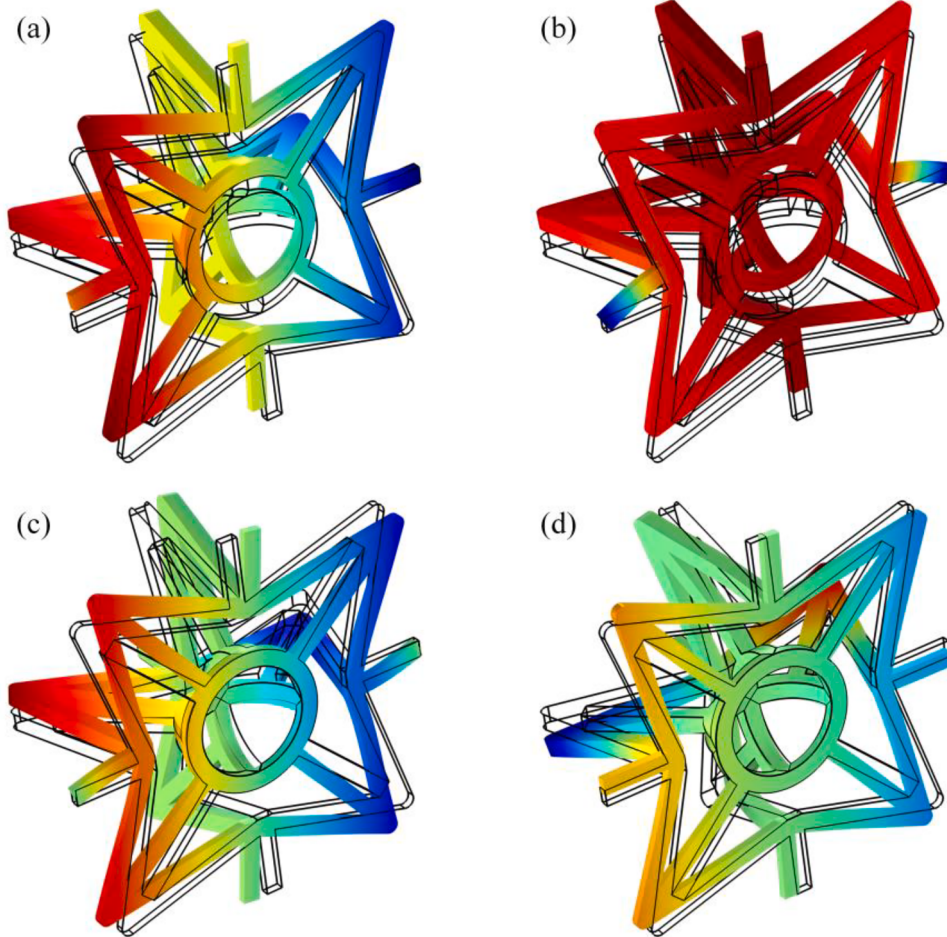


Fig. 13. Vibration patterns at the bounds of the transverse band gaps. For the first band gap: (a) the lower bound at position A and (b) the upper bound at position B in the top sub-figure of Fig. 11. For the second band gap: (c) the lower bound at position C and (d) the upper bound at position D in the top sub-figure of Fig. 11.

$$\begin{cases} \mathbf{d}_{out} = [\Phi_{b1} \quad U_{t1} \quad \Gamma_{t1} \quad \Phi_{b2} \quad U_{t2} \quad \Gamma_{t2}]^T \\ \mathbf{f}_{out} = [M_{x1} \quad Q_{y1} \quad T_1 \quad M_{x2} \quad Q_{y2} \quad T_2]^T \end{cases} \quad (49)$$

4.3. Dynamic response of the metamaterial

After the DSMs for straight and curved beams are derived, this subsection will show how to obtain the DSM for the entire system.

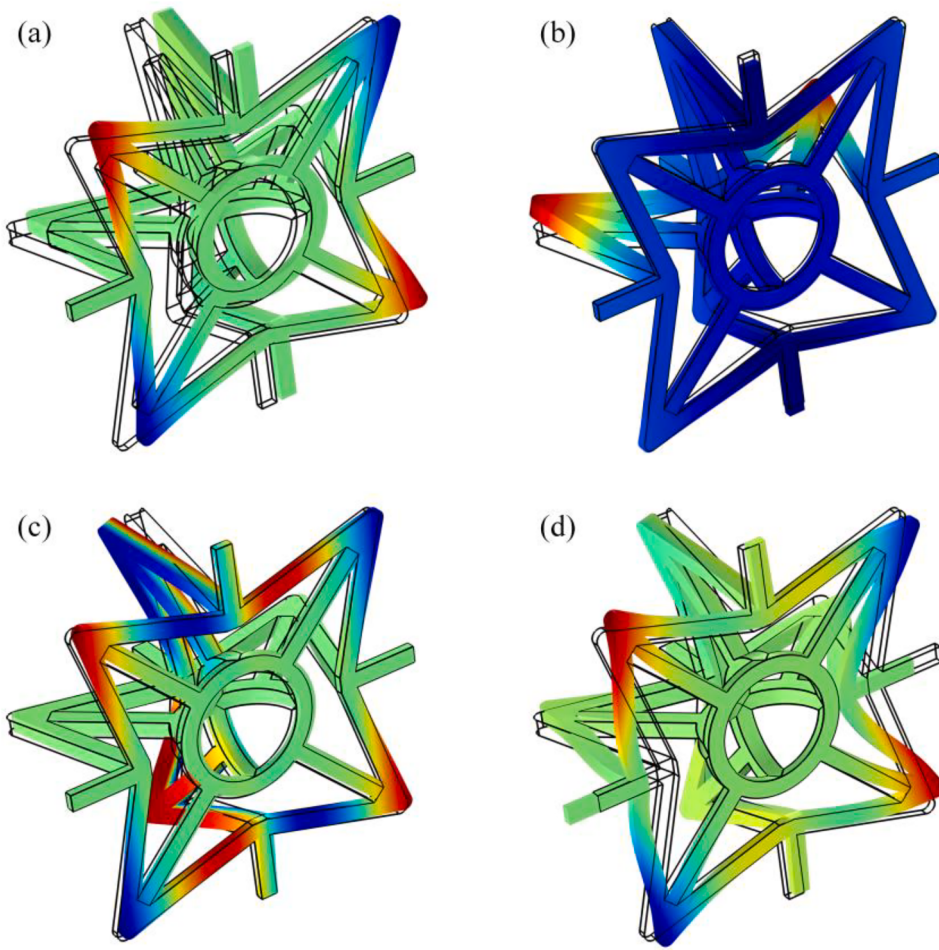


Fig. 14. Vibration patterns at the bounds of the longitudinal band gaps. For the first band gap: (a) the lower bound at position A' and (b) the upper bound at position B' in the bottom sub-figure of Fig. 11. For the second band gap: (c) the lower bound at position C' and (d) the upper bound at position D' in the bottom sub-figure of Fig. 11.

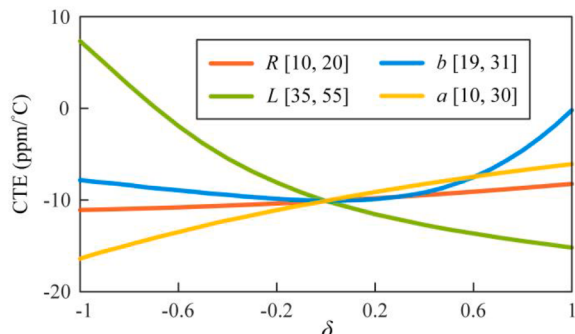


Fig. 15. Variations of the effective CTE with four main geometrical parameters. When other parameters remain unchanged, the variable of interest varies in a wide range as prescribed in the label. For description, the independent variables are normalized into $[-1, 1]$. Tuning L or b can adjust the effective CTE from negative to positive. In contrast, R and a are less sensitive to getting rid of negative CTE.

Furthermore, the dynamic response of the metamaterial will be analyzed to quantify its vibration suppression ability.

The global DSM of the proposed metamaterial can be constructed by following the same assembly procedure as widely adopted in the FEM. In the frequency response analysis, the external load is zero at the specified nodes, and no reaction force yields at free nodes. For the convenience of

imposing these boundary conditions, the standard governing equation is recast into

$$\mathbf{S}\mathbf{d} = \mathbf{r} \Rightarrow \begin{bmatrix} \mathbf{S}_s & \mathbf{S}_{sf} \\ \mathbf{S}_{sf}^T & \mathbf{S}_f \end{bmatrix} \begin{bmatrix} \mathbf{d}_s \\ \mathbf{d}_f \end{bmatrix} = \begin{bmatrix} \mathbf{r}_s \\ \mathbf{0} \end{bmatrix} \quad (50)$$

where \mathbf{S} is the DSM of the entire system; \mathbf{d} stands for the global displacement vector; \mathbf{r} denotes the reaction force. The subscripts "s" and "f" indicate the components associated with the specified and free nodes, respectively. Thus, the unknown variables are determined as

$$\begin{cases} \mathbf{d}_f = -\mathbf{S}_s^{-1}\mathbf{S}_{sf}^T\mathbf{d}_s \\ \mathbf{r}_s = (\mathbf{S}_s - \mathbf{S}_{sf}\mathbf{S}_f^{-1}\mathbf{S}_{sf}^T)\mathbf{d}_s \end{cases} \quad (51)$$

Regarding the vibration suppression performance evaluation, a harmonic excitation is imposed at the clamped end of the metamaterial to trigger transverse or longitudinal vibration. By examining the free-end vibration via Eq. (49), the transmittance of the metamaterial can be evaluated by

$$\tau(\omega) = 20\log(d_{out}/d_{in}) \quad (52)$$

where d_{out} and d_{in} are the vibration displacements at the output and input ends, respectively. It is clear from the logarithmic definition that the input vibration is suppressed at the output end when $\tau(\omega) < 0$. Furthermore, the band gap width [73], which is a crucial measure of vibration suppression capability, is also evaluated. As multiple band

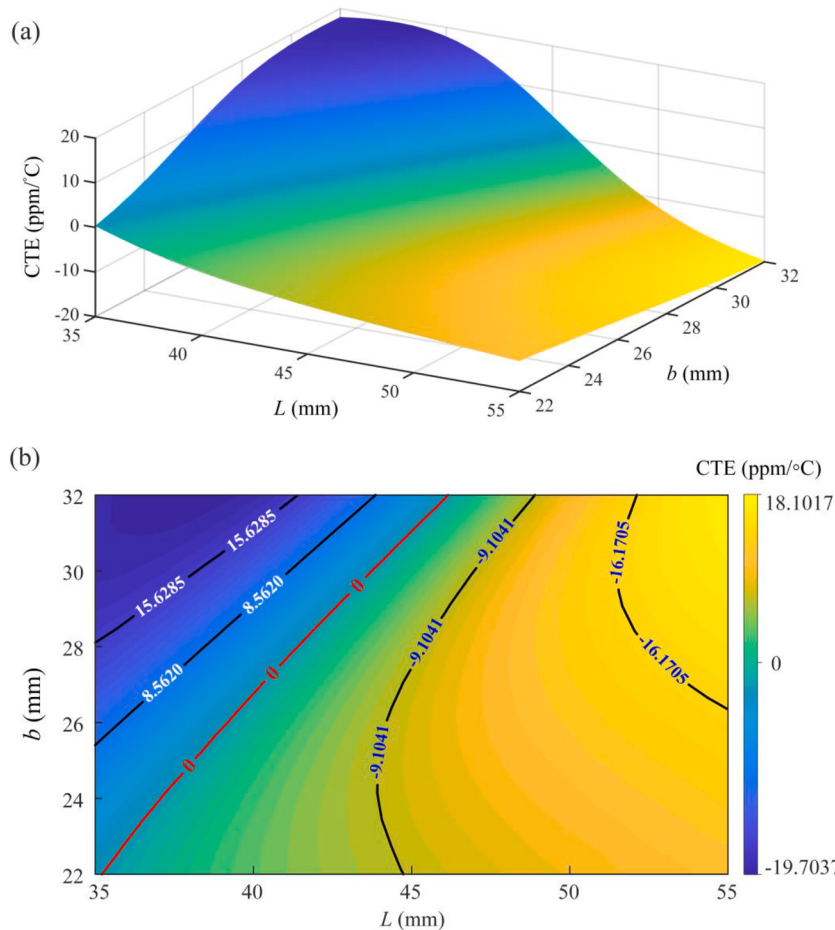


Fig. 16. Effective CTE of the metamaterial varying with the length of oblique struts L and the interior height b . (a) 3D-viewed mapping among the CTE, L , and b ; (b) Contour plots of CTE versus L and b . Noticeably, the effective CTE can be tuned from positive to negative. Specifically, the CTE increases monotonically from negative to positive with the increase of L . In addition, a transition point ($L=41.08$ mm) exists for the effect of b on the CTE. The effective CTE increases with the rise of b when L is less than 41.08 mm. However, when L exceeds 42.7 mm, the effective CTE initially declines before increasing with the increase of b . The red line in the second subplot provides all available combinations for achieving zero CTE.

Table 4
Geometric parameters of four metamaterials with zero CTE.

Geometric parameters of Metamaterials	#1	#2	#3	#4
Half-width of the interior lattice b (mm)	24.00	27.00	30.00	32.00
Length of the interior oblique struts L (mm)	37.06	40.27	43.74	46.16

gaps occur over different frequency ranges, this study adopts the central-frequency normalized bandwidth ΔG [43,74] to make a unified assessment, which is formulated as

$$\Delta G = \frac{2(f_u - f_l)}{f_u + f_l} \quad (53)$$

where f_u and f_l denote the upper and lower bound frequencies of the band gap, respectively.

5. Model verification and results discussion

This section will conduct FE simulations to verify the developed theoretical models in Sections 3 and 4. In addition to examining the CTE of the metamaterial, the transmittance response and band structure will be evaluated to quantify the vibration suppression performance.

5.1. Effective CTE of the metamaterial

In this subsection, the developed thermoelastic model will be validated for predicting the Effective CTE of the metamaterial. Furthermore, a comprehensive discussion on the thermal mismatch phenomenon will be provided to elucidate the underlying deformation mechanism.

The geometric parameters are set the same for the theoretical and simulation models, as listed in Table 1. Considering the CTE difference [24] and manufacturing feasibility [75], steel and Invar alloy are, respectively, used for the materials of exterior star-shaped re-entrant lattices and interior rudder-shaped reinforcement struts. The physical parameters of the two metallic materials are listed in Table 2.

To understand the deformation mechanism, the mechanical and thermal (temperature) loading are separately applied on the unit cell of the metamaterial. Fig. 6 depicts the simulated deformations under uniaxial and multiaxial compression conditions. As observed in Fig. 6(a), under the uniaxial compression in the z -direction, the metamaterial does not contract in the other two directions, which is different from the folding phenomenon of general re-entrant structures [62]. This is because the interior reinforcement struts weaken the planar contraction deformation of corners. Under the multiaxial compression with periodic boundary conditions, it can be seen from Fig. 6(b) that the exterior oblique lattices and interior curved struts are dominated by bending deformations, while the others are by stretching deformations. In addition, due to the cubic symmetry of the structure, the struts in the three orthogonal planes suffer the same deformations under the symmetric loading. Thus, essential parameters for describing the constitutive relations are reduced, making the design of such metamaterials easier.

Subject to a temperature increase of 200°C, the thermal-induced deformation of the unit cell is shown in Fig. 7. Similar to the case under the multiaxial compression in Fig. 6(b), the isotropic thermoelastic features also incorporate bending-dominated and stretching-dominated deformations. As will be demonstrated in the next section, such a combined deformation mechanism with the thermal mismatch effect can endow the metamaterial with a tunable CTE over a wide range.

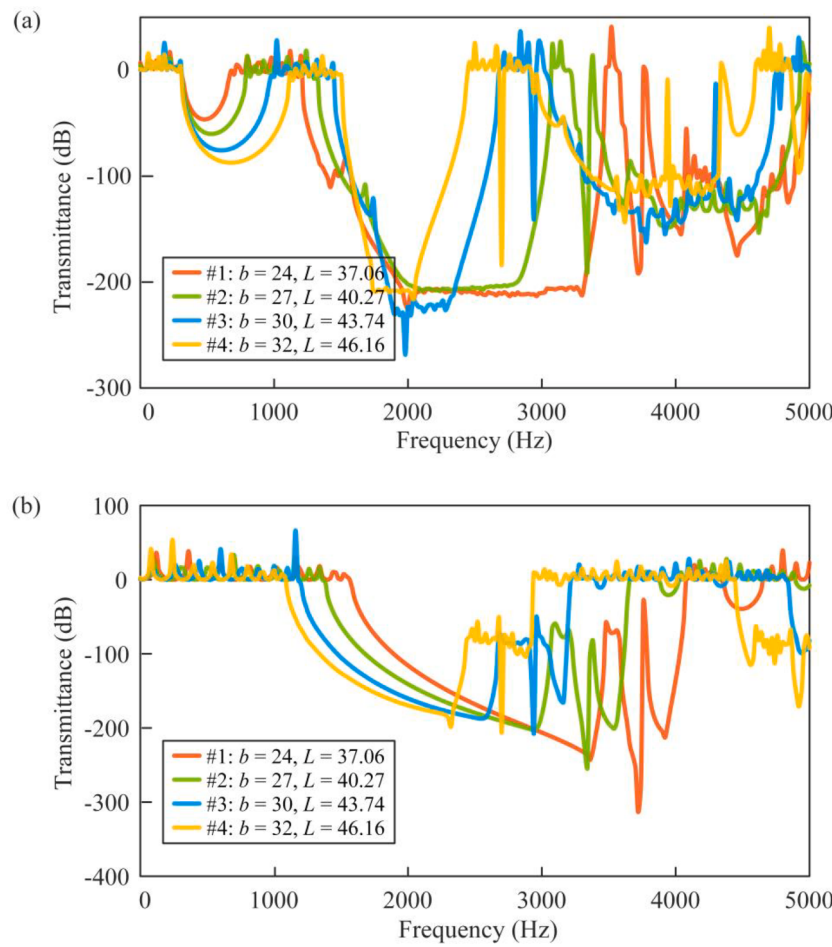


Fig. 17. Vibration propagation responses of the four metamaterials with zero CTE. (a) Transverse vibration; (b) longitudinal vibration. Every metamaterial exhibits three primary band gaps for the transverse vibration and a dominant band gap for the longitudinal vibration. More specifically, the start and end frequencies of band gaps are detailed in Table 5.

Table 5
Band gaps of the four dual-functional metamaterials.

Metamaterial	Performance	Transverse vibration	Longitudinal vibration
#1	Band gaps (Hz)	[298.31, 679.47], [1205.02, 3477.41], [3577.18, 4999.36]	[1563.78, 4079.83]
	Normalized bandwidth	0.78, 0.97, 0.33	0.89
#2	Band gaps (Hz)	[302.23, 792.86], [1320.12, 3073.98], [3385.59, 4938.32]	[1365.23, 3658.02]
	Normalized bandwidth	0.90, 0.80, 0.37	0.91
#3	Band gaps (Hz)	[304.00, 997.59], [1442.14, 2691.65], [3028.10, 4757.92]	[1183.46, 3216.49]
	Normalized bandwidth	1.07, 0.60, 0.44	0.92
#4	Band gaps (Hz)	[305.07, 1121.56], [1373.29, 2445.26], [2793.26, 4650.15]	[1083.18, 2935.90]
	Normalized bandwidth	1.14, 0.56, 0.50	0.92

Specifically, the thermal mismatch phenomenon arises from the unequal thermal strains experienced by two elements with different CTEs when subjected to heating without any constraints. As a result of the constraints imposed by the connection between the elements, the thermal strain redistributes to achieve an equilibrium state. This redistribution of strain leads to a change in the thermally-induced deformation of a freestanding beam, triggering thermal expansion or shrinkage of the fundamental element. Fig. 7 depicts the thermal mismatch effect on the metamaterial, with an enlarged view showing the actual thermal deformation.

In response to a temperature increase, all struts in the unit cell experience stretching. Since the CTE of the interior material is smaller than that of the exterior material, it is observed in Fig. 7(a) and (b) that

the thermal expansion deformations of the corner for the independent exterior and interior substructures are 0.10803 mm and 0.01089 mm, respectively, exhibiting a tenfold difference in magnitude. When the two substructures are connected, as depicted in Fig. 7(c), the thermal mismatch between them cause the interior substructure to exert pulling forces on the exterior one along the diagonal directions of metamaterial. As a result, the corner deformation is altered to 0.02857 mm. Moreover, these forces induce bending deformations in the exterior inclined beams, leading to inward elastic contractions at re-entrant points. Consequently, unlike thermal expansion, the metamaterial undergoes shrinkage along the three principal directions, leading to a reduction in its characteristic lengths.

Based on the above discussion, it can be summarized that the thermal

contraction behavior observed is a result of the combined thermal mismatch and re-entrant unfolding mechanisms. When the magnitude of elastic contraction surpasses that of microscopic thermal expansion, a metamaterial with a negative CTE can be achieved.

To verify the accuracy of the analytical model, several cases with different mechanical and temperature loadings are simulated to make comparisons. By measuring the elastic deformation between the two opposite connection nodes of the unit cell, both elastic deformation and thermal expansion are obtained via FE simulations and theoretical predictions. As shown in Fig. 8, the analytical and simulation results are in good agreement. Besides, linear responses are observed for the thermoelastic deformations, indicating that the elastic modulus and CTE are load-independent and temperature-independent within the linear regime.

According to the stress-strain relationship, the gradients of the curves in Fig. 8(a) and (b) are associated with the elastic modulus (E_{eff}) and CTE of the metamaterial. On this basis, the two physical parameters are determined and summarized in Table 3. Regarding the effective elastic modulus (E_{eff}) and CTE, the relative errors between the theoretical prediction and FE simulation are only -1.24% and -0.86% , respectively. The minor discrepancies verify that the developed analytical model is of satisfactory accuracy.

5.2. Dynamic response of the metamaterial

This section will validate the accuracy of the analytical model in characterizing vibration responses by comparing theoretical predictions with finite element simulations. On this basis, the band gap formation mechanisms will be further revealed for the metamaterial via the complex band structure and vibration mode analysis.

The dynamic analysis in this section considers a metamaterial consisting of 10 unit cells along the x -direction. As depicted in Fig. 9, both SEM and FEM are used to evaluate the transmittance characteristics of the metamaterial. Herein, COMSOL Multiphysics® is employed to build the corresponding FE model.

Fig. 9 compares the results from the developed SEM model and the FE simulation. The transmittance response predicted by the SEM agrees well with FE simulation results, indicating that the developed dynamic model has excellent prediction accuracy. Three band gaps, respectively, form over the frequency ranges of 1036.50–2217.57 Hz, 2633.99–3497.31 Hz, and 3942.71–4517.63 Hz. It can be calculated that the normalized bandwidths are $\Delta G_1=0.76$, $\Delta G_2=0.28$, and $\Delta G_3=0.14$, respectively. Compared with the meta-structures reported in [38,43], our proposed metamaterial produces three wider band gaps at low-frequency ranges, demonstrating a broadband low-frequency vibration suppression ability.

Solving the extreme values of multi-order eigenfrequencies within the first Brillouin zone is a well-known method to capture the features of band gaps. Moreover, performing the symmetric operation on the first Brillouin zone allows for extracting the irreducible Brillouin zone (IBZ), which represents the smallest undivided region of frequency and wavenumber. The dispersion relation of the elastic metamaterial can be completely characterized along the boundary of the IBZ. The proposed metamaterial is a 3D structure. We can obtain its band structure by sweeping the boundaries of the IBZ, as shown in Fig. 10. However, considering the complexity and abundance of information in the full band, we focus our study on the transverse and longitudinal wave propagation within a single row of unit cells in the metamaterial. To simplify the analysis, we reduce the 3D IBZ to a 1D IBZ and only consider the periodicity in the x -direction. This allows us to effectively capture the desired characteristics by sweeping the wavenumber along the path $\Gamma \rightarrow X$.

The band structure of the metamaterial, as shown in Fig. 11, is further investigated to figure out the band gap formation mechanisms. The Floquet periodic boundary condition is applied to the representative unit cell of the metamaterial without restrictions to wave types. We post-

processed the results to separate the transverse and longitudinal modes and plotted them in red and blue, respectively. In Fig. 11(a), we also appended the transverse transmittance spectra from Fig. 9. It can be found that the attenuation valleys form in between the red curves, indicating the good agreement between the band structure and transmittance analysis results. Based on the valley profile, we can infer the band gap type. For example, the first attenuation valley in Fig. 11(a) is nearly symmetric, and the valley bottom is smooth; thus, we can infer that a BS band gap forms the first attenuation valley. While the second attenuation valley in Fig. 11(a) is asymmetric and has downward spikes; thus we can infer that an LR band gap forms the second attenuation valley. In a similar way, we can also identify the types of longitudinal band gaps. The vibration attenuation valleys in Fig. 11(b) form in between those blue curves. The valley profiles imply that the first two are formed by the LR mechanism. The above conjectures based on the transmittance profile can be verified by the band structure analysis.

As depicted in Fig. 12, the imaginary part of the band structure, which provides attenuation information [76], is calculated to facilitate the mutual verification of the transmittance results. According to the distinct characteristics of two band gap mechanisms [77–79], it is known that the BS mechanism forms the first transverse band gap, as its imaginary part varies continuously and smoothly throughout the entire band gap. In contrast, the second transverse band gap, exhibiting a cusp (an abrupt change in slope) in its imaginary part, arises from the LR mechanism. In addition, we can observe two corners (I and II) at the bottom of the imaginary part of the second transverse band gap. This feature aligns well with the transmittance result shown in Fig. 11(a). Moreover, the first longitudinal band gap belongs to the LR type, as evidenced by the sharp attenuation valley at the bottom (annotation III in Fig. 11(b)), which accords with the spike-like feature of the imaginary part in Fig. 12.

Fig. 13 demonstrates the vibration patterns at the transverse band gap bounds, i.e., A, B, C and D in Fig. 11(a). Fig. 13(a) and (b) show the vibration patterns at the lower and upper bounds of the first band gap in Fig. 11(a). It can be seen that the whole structure is conducting consistent vibration motion, i.e., the color depth (indicating the displacement amplitude) varies smoothly from the left connection strut to the right side. It is well-known that the LR mechanism induces band gaps by producing out-of-phase motions in microstructures. However, no such sign is observed in Fig. 13(a). Moreover, the vibration pattern at the upper bound of the first band gap, as shown in Fig. 13(b), also has no sign of local resonance. Therefore, we can affirm that the first transverse band gap is formed based on the BS mechanism, which agrees with the prediction based on the transmittance profile. The things of the second band gap become different. Fig. 13(c) shows that the left connection strut is moving downward, while the struts at the flank are deforming upward. In contrast, the right connection strut is moving upward, and the struts at its flank are deforming downward. This vibration pattern clearly shows that the microstructures (the struts at the flank) are conducting out-of-phase motions with the host structure (connection struts). Similarly, an analogous vibration pattern is found in Fig. 13(d). Therefore, we can affirm that the second transverse band gap must be an LR type.

The vibration patterns at the bounds of the longitudinal band gaps, i.e., A', B', C' and D' in Fig. 11(b), are presented in Fig. 14. For the vibration patterns at the bounds of the first band gap, we can see that the connection struts almost do not vibrate. Either the frame struts (Fig. 14(a)) in the same vertical plane or the struts at the flank in the orthogonal horizontal plane (Fig. 14(b)) are conducting the most intense vibration to counteract the external excitation. The vibration pattern in Fig. 14(c) is similar. Fig. 14(d) shows that the connection struts are moving leftward, while the frame struts are deforming rightward. All these vibration patterns in Fig. 14 exhibit the signs of local resonance and out-of-phase motions in microstructures. Therefore, we affirm that the first two longitudinal band gaps are LR types, which agrees well with the identification results based on the transmittance profile.

5.3. Customizing the dual-functional metamaterial

After verifying the developed theoretical models, this section will demonstrate how the dual-functional metamaterial with zero CTE and vibration suppression performance can be obtained by adjusting geometric parameters.

As illustrated in Section 2, the geometric configuration of such metamaterials is determined by six independent parameters. Like previous studies [27,80], the thickness t of struts is selected as a dimensional reference of the whole system. Besides, the inclined angle θ of the interior beams is constrained at 45° to support the desired orthogonal symmetry. For the remaining four parameters, their effects on the CTE of the metamaterial over specific ranges are investigated and revealed in Fig. 15. The parameter search space, or the feasible range of parameters, is determined by the geometric constraints of the metamaterial. As designed in Fig. 1(a), threefold constraints must be satisfied: (I) the interior rudder-shaped structure should not interfere with the exterior star-shaped structure; (II) all corners of the unit cell must be confined within the overall height of the unit cell; and (III) the star-shaped structure should maintain its re-entrant configuration. Mathematically, the above geometric constraints are summarized as

$$\begin{cases} L\sin\theta > b > R + \frac{t}{2} \\ \beta = \frac{\pi}{2} - \theta + \arctan \frac{2b\cos\theta - t - t\sin\theta}{2L - 2b\sin\theta - t\cos\theta} < \frac{\pi}{2} \\ L + \frac{t}{2}\tan \frac{2\theta + 2\beta - \pi}{4} < a + b \end{cases} \quad (54)$$

To facilitate the parametric study, the feasible ranges of the parameters are further rounded into integers.

As can be observed in Fig. 15, the effective CTE is positively associated with the increase of R or a . Nevertheless, the CTE remains negative within the prescribed ranges, implying that R and a have no significant impact on CTE. The CTE sign of the metamaterial is more sensitive to L and b : over the variation range, the CTE changes from negative/positive to positive/negative. Hence, by appropriately selecting L and b , zero CTE metamaterials can be obtained without significantly altering their original geometric topology.

Subsequently, the coupling effects of the identified sensitive parameters (L and b) are further investigated to provide the parameter tuning scheme for achieving zero CTE. Fig. 16 shows how the effective CTE varies with the length of oblique struts (L) and the interior height (b). The other parameters remain constant, as prescribed in Table 1. It is seen from Fig. 16 that with the increase of L , the effective CTE monotonically changes from positive through zero to negative. Compared with the influence of L on the CTE, the relation between the interior height b and the CTE is more complicated. Specifically, when L is smaller than 41.08 mm, the CTE shows the same monotonicity as b . However, once $L > 41.08$ mm, the effective CTE initially decreases, then increases with the rise of b . Moreover, isotropic negative or positive CTE can be achieved with a magnitude as large as several to dozens of times that of the constituent materials.

According to Fig. 16(b), four zero CTE metamaterials with the parameters listed in Table 4 are chosen. Their band gap characteristics and vibration suppression abilities are investigated and compared. Fig. 17 plots the transmittances of the four zero CTE metamaterials. The band gaps are identified and summarized in Table 5. As observed in Fig. 17(a), three primary band gaps occur in the transverse vibration of the metamaterials. In particular, the larger the geometric dimensions, the wider the first and third band gaps, but the narrower the second band gap. Moreover, as the design parameters increase gradually, different influences are brought to the start frequencies of the three band gaps, with tendencies of being nearly unchanged, being shifted to the higher frequency and lower frequency, respectively. While the end frequencies of the three band gaps tend to decline, decline, and rise, respectively.

Regarding the longitudinal vibration of the four metamaterials, the transmittance responses, as shown in Fig. 17(b), reveal a dominant band gap within the frequency range below 5000 Hz. It is found that the bandwidth reduces with the increase of L and b , and the band gap shifts towards the lower frequency. These results indicate that the band gaps of the dual-functional metamaterial can also be tuned by adjusting the geometric parameters.

Furthermore, corresponding normalized bandwidths are calculated for the four metamaterials. As listed in Table 5, the normalized bandwidth for the transverse vibration reaches 0.33–1.14, and the bandwidth for the longitudinal vibration is more than 0.89. These multiple broadband gaps provide direct evidence that such metamaterials have exceptional vibration suppression ability [38,43]. In particular, it is worth noticing the fascinating feature that the transmittance valley at low frequencies, i.e., 298.31–1121.56 Hz, will be beneficial to the transverse vibration mitigation of engineering structures in practical applications [35].

6. Conclusions

This study has presented a novel dual-functional metamaterial with zero thermal expansion and broadband vibration suppression via rigorous theoretical analyses and in-depth technical discussions. The main concluding remarks are summarized below.

Leveraging the thermal mismatch and band gap effects, the proposed metamaterial has successfully achieved zero thermal expansion and broadband vibration suppression by incorporating star-shaped re-entrant lattices and locally rudder-shaped struts made of two-phase materials. Moreover, it has been verified that the developed theoretical models can accurately predict the thermoelastic properties and dynamic responses of the proposed metamaterial with complex geometric topology.

Comprehensive analyses have revealed the influences of geometric parameters on the effective CTE and vibration suppression performance of the dual-functional metamaterials. Particularly, the length of oblique struts and the interior height are found to have significant impacts on CTE. By tuning the two key parameters, the desired thermoelastic and vibration properties can be customized. It enables the attainment of isotropic negative or positive CTE with magnitudes several to dozens of times larger than the constituent materials, indicating its great potential for practical engineering applications. Meanwhile, the normalized bandwidth for transverse vibration ranges from 0.33 to 1.14, and the bandwidth for longitudinal vibration exceeds 0.89, demonstrating the capability for broadband vibration suppression.

To summarize, this study has provided valuable insights into the integration of dual functionalities in metamaterials and developed an efficient theoretical framework for designing multi-physics coupled meta-structures.

CRediT authorship contribution statement

Dewen Yu: Methodology, Software, Validation, Writing – original draft. **Guobiao Hu:** Investigation, Validation, Writing – review & editing. **Wei Ding:** Investigation, Formal analysis. **Yaowen Yang:** Conceptualization, Supervision, Writing – review & editing. **Jun Hong:** Supervision, Writing – original draft.

Declaration of Competing Interest

The authors declare that they have no known competing financial interests or personal relationships that could have appeared to influence the work reported in this paper.

Data availability

No data was used for the research described in the article.

Acknowledgment

The authors acknowledge the valuable discussions with Dr. Siyuan Sun (Tongji University, China), Huan Lu (Xi'an Jiaotong University,

China), and Yijiang Niu (University of Sheffield, UK). The generous assistance provided by Prof. Jingyi Li (Hainan University, China) in the simulation is greatly appreciated.

Appendix A. Force analysis of the representative volume element

Given the constraints and force diagrams as described in Fig. 2(d), the internal sub-structure satisfies the following equations:

$$\begin{cases} F_V = F_C; F_H = -F_B; \\ M_G = F_C(L\cos\theta - R) - F_B(L\sin\theta - R) + M_C - M_B. \end{cases} \quad (55)$$

On this basis, Table A. 1 presents the force equilibrium conditions of each strut under axial loadings, in which θ_j ($j = 1, 2, 4, 5$) is determined by the six independent geometric parameters.

Table A

1. Force equilibrium conditions of each strut under axial loadings.

No.	Struts	Force diagrams	Internal forces
1	AG		$F_{1a} = F_A \cos\theta_1 - F_y \sin\theta_1$ $F_{1s} = F_A \sin\theta_1 + F_y \cos\theta_1$ $M_{11} = M_A + F_A x_1 \sin\theta_1 + F_y x_1 \cos\theta_1$
2	DG		$F_{2a} = F_D \sin\theta_2 - F_x \cos\theta_2$ $F_{2s} = F_D \cos\theta_2 + F_x \sin\theta_2$ $M_{22} = M_D + F_D x_2 \cos\theta_2 + F_x x_2 \sin\theta_2$
3	EG		$F_{3a} = F_C \sin\theta + F_B \cos\theta$ $F_{3s} = F_C \cos\theta - F_B \sin\theta$ $M_{33} = -F_C x_3 \cos\theta + F_B x_3 \sin\theta + M_C - M_B - F_B (L \sin\theta - R) + F_C (L \cos\theta - R)$
4	BE		$F_{4a} = F_B \cos\theta_4$ $F_{4s} = F_B \sin\theta_4$ $M_{44} = M_B - F_B R (1 - \cos\theta_4)$
5	CE		$F_{5a} = F_C \sin\theta_5$ $F_{5s} = F_C \cos\theta_5$ $M_{55} = M_C - F_C R (1 - \cos\theta_5)$

References

- [1] Pietrosanti D, De Angelis M, Giaralis A. Experimental study and numerical modeling of nonlinear dynamic response of SDOF system equipped with tuned mass damper inerter (TMDI) tested on shaking table under harmonic excitation. *Int J Mech Sci* 2020;184:105762.
- [2] Zhang C, Mousavi AA, Masri SF, Gholipour G, Yan K, Li X. Vibration feature extraction using signal processing techniques for structural health monitoring: a review. *Mech Syst Signal Process* 2022;177:109175.
- [3] Yu D, Zhao Q, Guo J, Chen F, Hong J. Accuracy analysis of spatial overconstrained extendible support structures considering geometric errors, joint clearances and link flexibility. *Aerospace Technol* 2021;119:107098.
- [4] Fonseca LM, Rodrigues GV, Savi MA. An overview of the mechanical description of origami-inspired systems and structures. *Int J Mech Sci* 2022;223:107316.
- [5] Chandra M, Kumar S, Chattpadhyay S, Chatterjee S, Kumar P. A review on developments of deployable membrane-based reflector antennas. *Adv Space Res* 2021;68:3749–64.
- [6] Yu D, Yang Y, Hu G, Zhou Y, Hong J. Energy harvesting from thermally induced vibrations of antenna panels. *Int J Mech Sci* 2022;231:107565.
- [7] Boatti E, Vassios N, Bertoldi K. Origami metamaterials for tunable thermal expansion. *Adv Mater* 2017;29:1700360.
- [8] Yang N, Zhang M, Zhu R. 3D kirigami metamaterials with coded thermal expansion properties. *Extreme Mech Lett* 2020;40:100912.
- [9] Xie Y, Pei X, Yu J. Double-layer sandwich annulus with ultra-low thermal expansion. *Compos Struct* 2018;203:709–17.
- [10] Wang K, Chen J, Han Z, Wei K, Yang X, Wang Z, Fang D. Synergistically program thermal expansion and mechanical performances in 3D metamaterials: design-architecture-performance. *J Mech Phys Solids* 2022;169:105064.
- [11] Chen J, Xu W, Wei Z, Wei K, Yang X. Stiffness characteristics for a series of lightweight mechanical metamaterials with programmable thermal expansion. *Int J Mech Sci* 2021;202:106527.
- [12] Zhao S, Zhang Y, Chen D, Yang J, Kitipornchai S. Enhanced thermal buckling resistance of folded graphene reinforced nanocomposites with negative thermal expansion: from atomistic study to continuum mechanics modelling. *Compos Struct* 2022;279:114872.
- [13] Ha CS, Hestekin E, Li J, Plesha ME, Lakes RS. Controllable thermal expansion of large magnitude in chiral negative Poisson's ratio lattices. *Phys Status Solidi* 2015;252:1431–4.
- [14] Wei K, Peng Y, Wang K, Duan S, Yang X, Wen W. Three dimensional lightweight lattice structures with large positive, zero and negative thermal expansion. *Compos Struct* 2018;188:287–96.
- [15] Li Y, Chen Y, Li T, Cao S, Wang L. Hoberman-sphere-inspired lattice metamaterials with tunable negative thermal expansion. *Compos Struct* 2018;189:586–97.
- [16] Sleight AW. Thermal contraction. *Nature* 1997;389:923–4.
- [17] Jefferson G, Parthasarathy TA, Kerans RJ. Tailorable thermal expansion hybrid structures. *Int J Solids Struct* 2009;46:2372–87.
- [18] Lehman J, Lakes R. Stiff lattices with zero thermal expansion. *J Intell Mater Syst Struct* 2012;23:1263–8.
- [19] Ha CS, Plesha ME, Lakes RS. Simulations of thermoelastic triangular cell lattices with bonded joints by finite element analysis. *Extreme Mech Lett* 2017;12:101–7.
- [20] Lim TC. Negative thermal expansion structures constructed from positive thermal expansion trusses. *J Mater Sci* 2012;47:368–73.
- [21] Hopkins JB, Song Y, Lee H, Fang NX, Spadaccini CM. Polytope sector-based synthesis and analysis of microstructural architectures with tunable thermal conductivity and expansion. *J Mech Des* 2016;138:051401.
- [22] Xu W, Xiao X, Chen J, Han Z, Wei K. Program multi-directional thermal expansion in a series of bending dominated mechanical metamaterials. *Thin Walled Struct* 2022;174:109147.
- [23] Li J, Liu HT, Zhang ZY. Stiffness characteristics for bi-directional tunable thermal expansion metamaterial based on bi-material triangular unit. *Int J Mech Sci* 2023;241:107983.
- [24] Yu H, Wu W, Zhang J, Chen J, Liao H, Fang D. Drastic tailororable thermal expansion chiral planar and cylindrical shell structures explored with finite element simulation. *Compos Struct* 2019;210:327–38.
- [25] Wei K, Chen H, Pei Y, Fang D. Planar lattices with tailororable coefficient of thermal expansion and high stiffness based on dual-material triangle unit. *J Mech Phys Solids* 2016;86:173–91.
- [26] Wei K, Xiao X, Chen J, Wu Y, Li M, Wang Z. Additively manufactured bi-material metamaterial to program a wide range of thermal expansion. *Mater Des* 2021;198:109343.
- [27] Li X, Gao L, Zhou W, Wang Y, Lu Y. Novel 2D metamaterials with negative Poisson's ratio and negative thermal expansion. *Extreme Mech Lett* 2019;30:100498.
- [28] Tancogne-Dejean T, Mohr D. Elastically-isotropic elementary cubic lattices composed of tailored hollow beams. *Extreme Mech Lett* 2018;22:13–8.
- [29] Sajjad U, Rehman TU, Ali M, Park CW, Yan WM. Manufacturing and potential applications of lattice structures in thermal systems: a comprehensive review of recent advances. *Int J Heat Mass Transf* 2022;198:123352.
- [30] Ai L, Gao XL. Three-dimensional metamaterials with a negative Poisson's ratio and a non-positive coefficient of thermal expansion. *Int J Mech Sci* 2018;135:101–13.
- [31] Xu H, Farag A, Pasini D. Routes to program thermal expansion in three-dimensional lattice metamaterials built from tetrahedral building blocks. *J Mech Phys Solids* 2018;117:54–87.
- [32] Wang H, Yu H, Wang X, Zhou H, Lei H, Chen M, Guo X. Load-bearing sandwiched metastructure with zero thermal-induced warping and high resonant frequency: mechanical designs, theoretical predictions, and experimental demonstrations. *Mech Mater* 2023;177:104531.
- [33] Mukhopadhyay T, Adhikari S. Effective in-plane elastic properties of auxetic honeycombs with spatial irregularity. *Mech Mater* 2016;95:204–22.
- [34] Mukhopadhyay T, Adhikari S. Equivalent in-plane elastic properties of irregular honeycombs: an analytical approach. *Int J Solids Struct* 2016;91:169–84.
- [35] Yu H, Liang B, Zhao Z, Liu P, Lei H, Song W, Chen M, Guo X. Metamaterials with a controllable thermal-mechanical stability: mechanical designs, theoretical predictions and experimental demonstrations. *Compos Sci Technol* 2021;207:108694.
- [36] Zhao P, Zhang K, Qi L, Deng Z. 3D chiral mechanical metamaterial for tailored band gap and manipulation of vibration isolation. *Mech Syst Signal Process* 2022;180:109430.
- [37] Al Rifaie M, Abdulhadi H, Mian A. Advances in mechanical metamaterials for vibration isolation: a review. *Advances in Mechanical Engineering* 2022;14:16878132221082872.
- [38] An X, Lai C, Fan H, Zhang C. 3D acoustic metamaterial-based mechanical metatlattice structures for low-frequency and broadband vibration attenuation. *Int J Solids Struct* 2020;191:293–306.
- [39] Zhang L, Bai Z, Chen Y. Dual-functional hierarchical mechanical metamaterial for vibration insulation and energy absorption. *Eng Struct* 2022;271:114916.
- [40] Wen S, Xiong Y, Hao S, Li F, Zhang C. Enhanced band-gap properties of an acoustic metamaterial beam with periodically variable cross-sections. *Int J Mech Sci* 2020;166:105229.
- [41] El-Borgi S, Fernandes R, Rajendran P, Yazbeck R, Boyd J, Lagoudas D. Multiple bandgap formation in a locally resonant linear metamaterial beam: theory and experiments. *J Sound Vib* 2020;488:115647.
- [42] Krödel S, Delpero T, Bergamini A, Ermanni P, Kochmann DM. 3 D Auxetic Microlattices with Independently Controllable Acoustic Band Gaps and Quasi-Static Elastic Moduli. *Adv Eng Mater* 2014;16:357–63.
- [43] Yu D, Hu G, Guo Z, Hong J, Yang Y. Topological interface state formation in an hourglass lattice sandwich meta-structure. *Int J Mech Sci* 2023;246:108170.
- [44] Dong J, Chen W, Zeng Z, Qin QH, Xiao Y. Analysis of wave band gaps in mechanical metamaterial based on Nelder-Mead method. *Eng Anal Bound Elem* 2019;103:109–15.
- [45] Chen W, Tian X, Gao R, Liu S. A low porosity perforated mechanical metamaterial with negative Poisson's ratio and band gaps. *Smart Mater Struct* 2018;27:115010.
- [46] Bao B, Lallart M, Guyomar D. Manipulating elastic waves through piezoelectric metamaterial with nonlinear electrical switched Dual-connected topologies. *Int J Mech Sci* 2020;172:105423.
- [47] Wang Y, Yang J, Chen Z, Gong X, Du H, Zhang S, Li W, Sun S. Investigation of a novel MRE metamaterial sandwich beam with real-time tunable band gap characteristics. *J Sound Vib* 2022;527:116870.
- [48] Zhou X, Sun Y, Yang S, Bian Z. Band gap manipulation on P-wave propagating in functionally graded phononic crystal by periodical thermal field. *Int J Mech Sci* 2021;212:106817.
- [49] Xie L, Xia B, Liu J, Huang G, Lei J. An improved fast plane wave expansion method for topology optimization of phononic crystals. *Int J Mech Sci* 2016.
- [50] Dal Poggetto VF, Serpa AL. Elastic wave band gaps in a three-dimensional periodic metamaterial using the plane wave expansion method. *Int J Mech Sci* 2020;184:105841.
- [51] Hu G, Austin AC, Sorokin V, Tang L. Metamaterial beam with graded local resonators for broadband vibration suppression. *Mech Syst Signal Process* 2021;146:106982.
- [52] Wu ZJ, Li FM, Zhang C. Vibration band-gap properties of three-dimensional Kagome lattices using the spectral element method. *J Sound Vib* 2015;341:162–73.
- [53] U. Lee, Spectral element method in structural dynamics, John Wiley & Sons 2009.
- [54] Song Y, Kim S, Park I, Lee U. Dynamics of two-layer smart composite Timoshenko beams: frequency domain spectral element analysis. *Thin Walled Struct* 2015;89:84–92.
- [55] Hajheidari H, Mirdamadi HR. Frequency-dependent vibration analysis of symmetric cross-ply laminated plate of Levy-type by spectral element and finite strip procedures. *Appl Math Model* 2013;37:7193–205.
- [56] Prasad R, Baxy A, Banerjee A. Wave propagation in tapered periodic curved meta-frame using floquet theory. *J Vib Acoust* 2022;144.
- [57] Prasad R, Baxy A, Banerjee A. Two-dimensional in-plane elastic waves in curved-tapered square lattice frame structure. *J Appl Mech* 2022;89.
- [58] Baxy A, Prasad R, Banerjee A. Elastic waves in layered periodic curved beams. *J Sound Vib* 2021;512:116387.
- [59] Yu X, Zhou J, Liang H, Jiang Z, Wu L. Mechanical metamaterials associated with stiffness, rigidity and compressibility: a brief review. *Prog Mater Sci* 2018;94:114–73.
- [60] Dove MT. Flexibility of network materials and the Rigid Unit Mode model: a personal perspective. *Philos Trans R Soc A* 2019;377:20180222.
- [61] Wei K, Peng Y, Qu Z, Pei Y, Fang D. A cellular metastructure incorporating coupled negative thermal expansion and negative Poisson's ratio. *Int J Solids Struct* 2018;150:255–67.
- [62] Ai L, Gao XL. Metamaterials with negative Poisson's ratio and non-positive thermal expansion. *Compos Struct* 2017;162:70–84.
- [63] Li J, Yang Q, Wei Y, Huang N, Tao R. A synergistic design of composite metamaterial with drastically tailororable thermal expansion and Poisson's ratio. *Compos Struct* 2021;275:114446.
- [64] Lu ZQ, Zhao L, Ding H, Chen LQ. A dual-functional metamaterial for integrated vibration isolation and energy harvesting. *J Sound Vib* 2021;509:116251.

- [65] Xu W, Lv S, Bai L, Qi W, Wang W. Multifunctional design of triangular lattice metamaterials with customizable thermal expansion and tunable bandgap properties. *J Appl Phys* 2021;130:085106.
- [66] Lv S, Xu W, Bai L, Qi W, Wang W. Thermal tuning of band gap properties in planar stretch-dominated lattices with tailororable coefficient of thermal expansion. *Appl Phys A* 2021;127:425.
- [67] Yuan X, Chen M, Yao Y, Guo X, Huang Y, Peng Z, Xu B, Lv B, Tao R, Duan S. Recent progress in the design and fabrication of multifunctional structures based on metamaterials. *Curr Opin Solid State Mater Sci* 2021;25:100883.
- [68] Yin S, Guo W, Wang H, Huang Y, Yang R, Hu Z, Chen D, Xu J, Ritchie RO. Strong and tough bioinspired additive-manufactured dual-phase mechanical metamaterial composites. *J Mech Phys Solids* 2021;149:104341.
- [69] Meng Z, Liu M, Zhang Y, Chen CQ. Multi-step deformation mechanical metamaterials. *J Mech Phys Solids* 2020;144:104095.
- [70] Peng XL, Bargmann S. Tunable auxeticity and isotropic negative thermal expansion in three-dimensional lattice structures of cubic symmetry. *Extreme Mech Lett* 2021;43:101201.
- [71] Dong SB, Alpdogan C, Taciroglu E. Much ado about shear correction factors in Timoshenko beam theory. *Int J Solids Struct* 2010;47:1651–65.
- [72] Tüfekçi E, Arpacı A. Exact solution of in-plane vibrations of circular arches with account taken of axial extension, transverse shear and rotatory inertia effects. *J Sound Vib* 1998;209:845–56.
- [73] Chen Y, Wu B, Su Y, Chen W. Effects of strain stiffening and electrostriction on tunable elastic waves in compressible dielectric elastomer laminates. *Int J Mech Sci* 2020;176:105572.
- [74] Banerjee A, Adhikari S, Hussein MI. Inertial amplification band-gap generation by coupling a levered mass with a locally resonant mass. *Int J Mech Sci* 2021;207:106630.
- [75] Yakout M, Elbestawi M, Veldhuis SC. A study of thermal expansion coefficients and microstructure during selective laser melting of Invar 36 and stainless steel 316L. *Addit Manuf* 2018;24:405–18.
- [76] Miao Z, Li J, Li S, Ma Q. Complex band structure of 2D piezoelectric local resonant phononic crystal with finite out-of-plane extension. *Appl Sci* 2022;12:7021.
- [77] Bhatt A, Banerjee A, Adhikari S. Closed-form solutions for attenuation peaks and band boundaries of general monocoupled systems. *J Sound Vib* 2022;541:117318.
- [78] Bhatt A, Banerjee A. Flexural wave propagation in rigid elastic combined metabeam. *J Vib Acoust* 2023;145:011006.
- [79] Mead DJ. The forced vibration of one-dimensional multi-coupled periodic structures: an application to finite element analysis. *J Sound Vib* 2009;319:282–304.
- [80] Lu H, Wang X, Chen T. Enhanced stiffness characteristic and anisotropic quasi-static compression properties of a negative Poisson's ratio mechanical metamaterial. *Thin Walled Struct* 2022;179:109757.